Tuning of type-I and type-II mechanisms for visible light degradation in tris(styryl)benzene-sensitized TiO$_2$ nanoparticles

Josefa Ortiz-Bustos[a], Isabel del Hierro[a], Antonio Sánchez-Ruiz[b,c], Joaquín C. García-Martínez[b,c]*, Yolanda Pérez[a,d]*

[a]Departamento de Biología y Geología, Física y Química Inorgánica. Escuela Superior de Ciencias Experimentales y Tecnología. Universidad Rey Juan Carlos. 28933 Móstoles (Madrid), Spain.

[b]Centro Regional de Investigaciones Biomédicas (CRIB), C/Almansa s/n, 02008, Albacete, Spain

[c]Departamento de Química Inorgánica, Orgánica y Bioquímica, Facultad de Farmacia, Universidad de Castilla-La Mancha, Avda. José María Sánchez Ibáñez s/n, 02008 Albacete, Spain

[d]Advanced Porous Materials Unit, IMDEA Energy Institute, Av. Ramón de la Sagra 3, 28935 Móstoles, Madrid, Spain

E-mail: yolanda.cortes@urjc.es, JoaquinC.Garcia@uclm.es

Abstract

The visible light activation of TiO$_2$ have been carried out by sensitization method using robust and metal-free tris(styryl)benzene (TSB) compounds as efficient sensitizers, which can be easily prepared. TSB compounds decorated with three carboxylic acid (**3$_{COOH}$**) or aldehyde (**3$_{CHO}$**) groups have been tightly incorporated to the surface of TiO$_2$ nanoparticles through different chemical linkage. The synthesized materials have been deeply characterized by different spectroscopic and analytical techniques to investigate the effect of TSB sensitizers in the photocatalytic properties of TiO$_2$. Comparative and exhaustive optical studies have been performed in solution between TSB compunds and sensitized TiO$_2$ nanoparticles, computational studies have been also carried to shed light on the sensitization process. The results reveal different mechanisms of sensitization (Type I and Type II) between the **3$_{CHO}$** and **3$_{COOH}$** compounds and TiO$_2$ nanoparticles. Thus, the influence of electronic injection mechanism (direct or indirect) has been

studied and mechanisms have been proposed for photodegradation of dye pollutants under UV and visible irradiation. TiO_2 nanoparticles sensitized with **3_{COOH}** (**TiO_2-3_{COOH}**) exhibited the best visible photocatalytic activity with a removal efficiency around 98% for methylene blue in 30 min and methyl orange after 60 min.

1. Introduction

The dumping of organic contaminants from pharmaceutical, textile, agricultural and cosmetic industries into aquatic environment can cause adverse human health and environmental effects [1]. In particular, textile, leather and paper industries consume large amounts of dyes in their products and a percentage of these dyes are released into the effluents [2], which can produce harmful effects since they are toxic, mutagenic, carcinogenic and teratogenic [3]. Conventional methods for wastewater treatment are not efficient to remove these dyes, and alternative methodologies are being currently developed. Among them, titanium dioxide photocatalysis has been successfully used for the elimination of different types of pollutants from water and it is regarded as an environmental-friendly method [4].

Visible light activation of TiO_2 can be carried out by several strategies [5], one of them being the sensitization method, widely utilized in solar cells [6] and water-splitting [7]. The sensitization process proceeds by two mechanisms depending on the electron injection from the dye to the TiO_2: one is the type I or two-steps mechanism, which involves photoexcitation of the dye followed by electron injection via LUMO of dye to the conduction band (CB) of TiO_2. The other one is the type II, or one-step mechanism, in which charge transfer occurs from the HOMO of dye molecule to the CB of TiO_2 forming ligand-to-metal charge transfer (LMCT) complexes on TiO_2. Thus, Type I sensitization is also referred as an indirect electron injection or dye-sensitization and type II as direct electron injection or LMCT sensitization. It should be noted that the electron injection can be more effective when the dye is covalently bonded to the surface of TiO_2 [8]. Additionally, LMCT sensitizers have been effectively used for solar energy conversion and environment remediation [9].

In the sensitization of TiO_2 for photodegradation of dye pollutants, most reports are focused on the use Type I sensitizers such as metalloporphyrins [10], porphyrins [11], poly-o-phenylenediamine [12], curcumine [13], benzimidazolone Yellow H3G [14] and chlorophyll-Mg [15] among others. There are a few examples of LMCT sensitization on TiO_2 for photodegradation of dye pollutants. Chen et al. [16] modified TiO_2 with toluene 2,4-diisocyanate to form an organic complex (N-(3-amino-4-methyl)phenylcarbamate) bonded to the surface of TiO_2 which degraded 34 % of methyl orang (MO) in 240 min under visible irradiation. Jiang et al. [17] prepared TiO_2 particles attached on the surface

of mesoporous phenolic resol to attain a charge transfer complex between TiO_2 and phenolic resol. This material degraded 70 % of MO in 10 h. In this sense, to the best of our knowledge, the influence of the type of sensitization mechanism using the same type of sensitizer has not yet been studied for photodegradation of dye pollutants. Other photocatalyst systems have been efficiently used in the degradation of organic dyes such as CuI nanoestructures [18], $TbFeO_3$ ceramic nanostructures [19], AgI/C_3N_4 nanocomposites [20] and ZIF-8 nanomaterials [21].

Here, we have chosen tris(styryl)benzene (TSB) compounds decorated with two different groups as metal-free sensitizers. The TSB compound with carboxylic acid groups (**3$_{COOH}$**) which is bonded to the TiO_2 surface via carboxylate group through the bidentate o monodentate coordination (**TiO$_2$-3$_{COOH}$**) and the aldehyde derivative (**3$_{CHO}$**) via imine bond formation through stable siloxane surface bonds to TiO_2 (**TiO$_2$-APTS-3$_{CHO}$**). In order to study the type of sensitization between the TSB compounds and TiO_2 nanoparticles, computational studies have been carried out and optical properties have been measured for free TSB compounds and the sensitized TiO_2 nanoparticles. Photocatalytic activity of TiO_2 samples have been studied for dye pollutants with different chemical structure, a cationic dye (methylene blue) and an anionic dye (methyl orange) under irradiation of UV or visible lights. Both sensitized TiO_2 nanoparticles were more effective for the degradation of dye pollutants than unmodified TiO_2. Finally, different mechanisms for photocatalytic degradation were proposed depending on the UV or visible light irradiation.

2. Experimental Section

2.1. Materials

Titanium (IV) isopropoxide, (3-Aminopropyl)triethoxysilane, 1,3,5-tris(bromomethyl)benzene, triethyl phosphite, potassium *tert*-butoxide, methyl 4-formylbenzoate, 4-(diethoxymethyl)benzaldehyde, and nitric acid 65 % were purchased from Merck. Methylene blue and methyl orange were purchased from Scharlab. Solvents (toluene, tetrahydrofuran, ethanol, methanol and 2-propanol) were acquired from SDS and toluene and tetrahydrofuran were distilled from drying agents. MilliQ water was used in experiments.

2.2. Synthesis of 1,3,5-tris(styryl)benzene compounds

4

Compounds 3_{COOH} and 3_{CHO} were used and prepared according with described literature and characterized by standards techniques in organic chemistry such as NMR, FTIR and MS [22-24]. Briefly, this methodology is based on Horner-Wadsworth-Emmons reaction among the corresponding phosphonates, the appropriate aldehyde and potassium *tert*-butoxide in THF (see Supporting Information). The *trans* stereochemistry of the double bonds was unequivocally established on the basis of the coupling constant for the vinylic protons in the ^{1}H NMR spectra ($J \approx 16$ Hz).

2.3. Functionalization of TiO₂ nanoparticles with 3$_{COOH}$ (TiO₂-3$_{COOH}$)

TiO$_2$ nanoparticles were prepared following a published procedure by our group [25]. Prior to the functionalization reaction, 1.5 g of TiO$_2$ material was dehydrated under vacuum at 120 °C for 6 h. In a typical post-synthetic method, TiO$_2$ nanoparticles were dispersed in 45 mL of dry tetrahydrofuran with stirring and under nitrogen atmosphere. Simultaneously, a 5 % molar ratio of 3_{COOH} were dissolved in 5 mL of dry tetrahydrofuran and the solution was added to the TiO$_2$ suspension and the mixture heated at 50 °C during 6 h. After, the suspension was filtered off and washed with tetrahydrofuran. The resulting yellow solid was dried under vacuum and denoted as **TiO₂-3$_{COOH}$**.

2.4. Functionalization of TiO₂ nanoparticles with 3$_{CHO}$ (TiO₂-APTS-3$_{CHO}$)

Like previous procedure, TiO$_2$ nanoparticles were dehydrated under vacuum at 120 °C for 6 h with the aim to remove residual physisorbed water. Then, TiO$_2$ support was modified with an amino group by post-synthesis grafting. Thus, 1 g of TiO$_2$ was suspended in 50 mL of dry toluene and 10 % molar ratio of (3-aminopropyl)triethoxysilane was added and the reaction was stirring at 110 °C for 24 h and kept under inert atmosphere. The suspension was filtered, washed with toluene and methanol and dried under vacuum at 90 °C during 5h. Then, 1 g of TiO$_2$-APTS was dispersed in dry THF and, at the same time, 0.5 mmol of 3_{CHO} was also dissolved in dry THF. Finally, the dispersions were mixed, kept stirring at room temperature during 24 h. The suspension was filtered and washed with THF and the resulting solid was dried under vacuum. The yellow solid obtained was labelled as **TiO₂-APTS-3$_{CHO}$**.

2.5. Photocatalytic degradation of aqueous methylene blue (MB) and methyl orange (MO)

Photocatalytic degradations of methylene blue were carried out with 20 mg of TiO$_2$ sample dispersed in 50 ml of a MB solution with a concentration of 0.04 mM. Some

experiments were carried out with 8 mg of photocatalyst in 20 ml of MB solution to keep the same ratio catalyst/volume. After 1 h of stirring in darkness to ensure the adsorption – desorption equilibrium, the suspensions were lighted up with different lamps, UV light at λ = 365 nm and 36 W, 60 W LED lamp or visible light at λ > 420 nm and 300 W.

Same procedure was performed for the photocatalytic degradation of methyl orange pollutant. Both MB and MO degradation reactions were followed using a spectrophotometer (SP-830) at maximum wavelengths of MB (664 nm) or MO species (464 nm).

2.6. Characterization Techniques

X-Ray diffraction (XRD) patterns of the catalysts were acquired on a Phillips Diffractometer model PW3040/00 X'Pert MPD/MRD at 45 KV and 40 mA, using Cu-Kα radiation (λ=1.5418 Å). Micromeritics TriStar 3000 analyser was used to record the adsorption-desorption isotherms of nitrogen N_2. Thermogravimetric analysis (TGA) was obtained with a Star system Mettler Thermobalance in the temperature range from 40 to 700 °C at 5 °Cmin^{-1}. FT-IR spectra were performed on a Varian Excalibur Series 3100 – UMA 600 spectrometer in Attenuated Total Reflectance (ATR) mode. ^{13}C NMR CP-MAS spectra were recorded on a Bruker Avance III/HD Spectrometer operating at 100.52 MHz carbon frequency (3 μs 90° pulse, 4096 transients, spinning speed of 12 MHz, contact time 3 ms, pulse delay 5 s). Diffuse Reflectance ultraviolet-visible (DRUV-Vis) spectra were performed using a Varian Cary 500 spectrophotometer. Transmission electron microscope (TEM) studies were performed using a 2100 JEM (JEOL) electron microscope operating at 200 kV. Specimens for TEM observation were prepared by depositing a drop of aqueous solutions of the samples onto a holey carbon grid (EMS). Scanning Electron Microscope in high resolution (SEM-FEG) was accomplished using a Nova NanoSEM 230 microscope. The zeta potential values were obtained by suspending of modified nanoparticles in a buffered solution (0.1 mgmL^{-1}) at pH = 7.4 using Nanoplus Zeta Potential and Nano Particle Analyzer from Micromeritics. Absorption and fluorescence spectra of all compounds were acquired in different solvents at 25 °C. Quartz cuvettes (Hellma Analytics) of 10 mm were employed for those measurements. UV-vis absorption spectra were acquired in a V-650 (Jasco) spectrophotometer and with a scan rate of 600 nm min^{-1}. A Peltier accessory was employed to control the temperature of the spectrophotometer measuring cell. Fluorescence spectra were acquired in a FS5

(Edinburgh Instruments) spectrofluorometer equipped with a Xe lamp of 150 W as the light source and a time correlated single photon counting (TCSPC) detector. A temperature-controlled cuvette holder, TLC 50 (Quantum Northwest), was used for the measurements. The excitation wavelength was selected at the maximum absorption wavelength, and the excitation and emission slits were opened to 1 and 1 nm, respectively. The step and dwell time were 1 nm and 0.1 s, respectively. Theoretical calculations for the computation of the molecular structure and electronic properties of the studied systems were conducted using the Gaussian 09 package (Release D.01) [26]. Total organic carbon (TOC) was determined to measure the amount of organic carbon found in dye molecules that was mineralized to CO_2 + H_2O during photodegradation reaction. The mineralization efficiency was calculated by estimating the total organic carbon (TOC) using a combustion/non-dispersive infrared gas analyzer model TOC-V from Shimadzu after 2 hours of reaction by the equation:

$$\% \, Mineralization = \frac{TOC_{initial} - TOC_{final}}{TOC_{initial}} * 100$$

2.7. Electrochemical measurements

The electrochemical studies were carried out using a conventional three-electrode cell. First, 0.1 M of hexafluorophospate tetrabutylammonium was dissolved in dry THF as a supporting electrolyte. In this solution, 1 mM of each TSB compound was dissolved to obtain their electrochemical data. A glassy carbon electrode was employed as a working electrode, platinum as a reference electrode and a Pt wire was also used as a counter. Ferrocene (Fc/Fc^+) was used as an internal standard in the same concentration that the dye in THF mixture. For the solid samples, a modified carbon paste electrodes (MCPE) were prepared with the same procedure that in previous works [27].

Electrochemical impedance spectroscopy (EIS) data were recorded by using a potentiostat/galvanostat with an impedance module with AC signal of 10 mV amplitude in the frequency range between 0.01 Hz and 100 kHz in potentiostatic conditions. The electrode potentials were measured against a saturated Ag/AgCl(s) reference electrode. All the measurements were done in 0.2 mol L^{-1} Na_2SO_4 solution using deionized water.

3. Results and discussion

3.1. Synthesis and Characterization

Here, tris(styryl)benzene derivates with three carboxylic acid groups (3_{COOH}) or three formyl groups (3_{CHO}) were synthesized according to previously reported procedure [24]. The sensitized TiO_2 nanoparticles, **TiO_2-3_{COOH}**, were prepared by a surface modification method of TiO_2 nanoparticles with 3_{COOH} compound and **TiO_2-APTS-3_{CHO}** material by the reaction of aminopropyl-modified TiO_2 nanoparticles with the aldehyde derivative, 3_{CHO}, via formation of an imine bond.

The X-ray diffraction patterns of unmodified TiO_2 and sensitized TiO_2 nanoparticles are shown in Fig. 1. The spectrum of bare TiO_2 exhibited main peaks corresponding to anatase phase and minor peaks due to formation of brookite phase. The spectra of modified TiO_2 nanoparticles showed the same pattern, indicating that the crystal structure was maintained after the sensitization process. The amount of brookite was calculated from $I_{brookite}(121)$ /($I_{brookite}$ (120) + $I_{anatase}$ (101) ratio [28] resulting around 19 % in all TiO_2 samples. Accordingly, the combination of anatase and brookite phases in TiO_2 can contribute to increase visible light photocatalytic activity compared to anatase TiO_2 since the electrons in the CB in brookite can be transferred into the CB of anatase [29]. Also, a slight shifting and broadening in XRD peak of (101) reflection (Fig. S1) was observed for sensitized TiO_2 samples, in comparison with bare TiO_2 nanoparticles. This might be due the incorporation of TSB compounds [30]. Additionally, the mean crystallite size of the nanoparticles was calculated from the (101), (105) and (004) peaks of anatase using the Scherrer's equation (Table 1). Bare TiO_2 sample presented 7.58 nm of crystallite size, which increased to 7.74 and 7.80 nm when TiO_2 was modified with 3_{COOH} and 3_{CHO} moieties, respectively. TEM micrographs of sensitized TiO_2 samples (Fig. S2) showed roughly rounded particles with slight aggregation. The high magnification TEM images (Fig. S2b and S2d) showed, as expected, the occurrence of mesoporous structure in the sensitized TiO_2 samples. The morphological structure of the TiO_2 samples was also studied by SEM analysis (Fig. S3). The SEM micrographs showed a slight increase of the nanoparticle's size after sensitization of TiO_2 with TSB compounds, confirming the data obtained from XRD analysis using the Scherrer's equation.
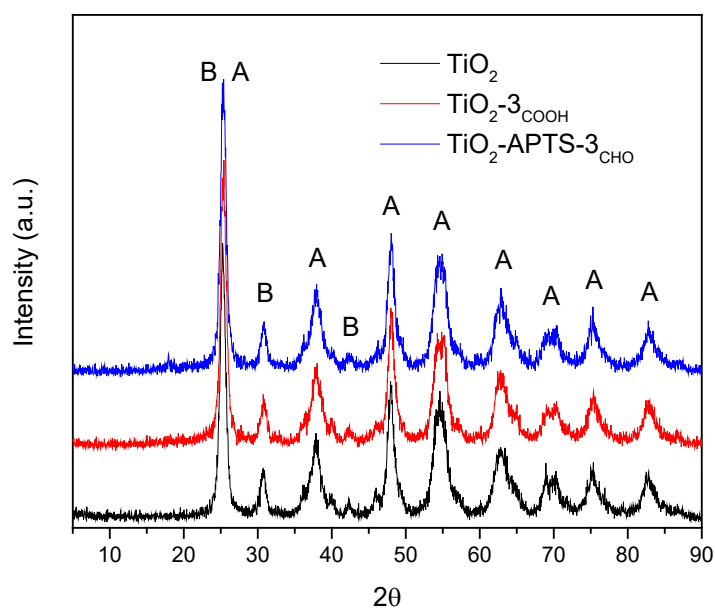
Fig. 1. X-Ray diffractograms of TiO_2 and sensitized TiO_2 samples (A=Anatase, B=Brookite)

Fig. 2 shows the nitrogen adsorption-desorption isotherms of TiO_2 materials. As can be seen, all materials exhibited type IV isotherms with hysteresis loop type H2 according to the IUPAC classification which are indicative of mesoporous materials. The sensitization of TiO_2 material reduced textural properties such as specific surface area, average BJH pore diameter and pore volume values (Table 1) due to the incorporation of organic compounds on the surface of TiO_2 nanoparticles. The BJH pore size distributions (Fig. S4) revealed a relatively narrow mesopores distribution centred at 8.7 nm for TiO_2 and at 7.3 and 7.1 nm for **TiO_2-3$_{COOH}$** and **TiO_2-APTS-3$_{CHO}$**, respectively.
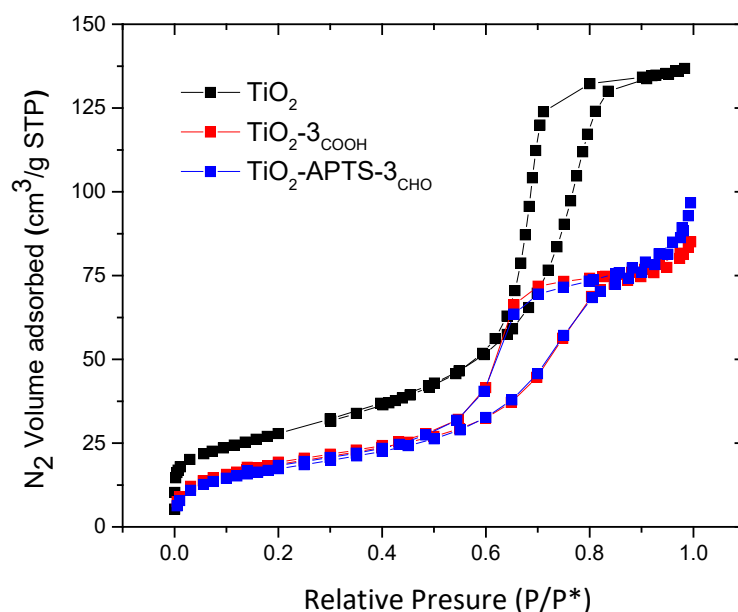
1

2   **Fig. 2.** Adsorption-desorption isotherms of TiO$_2$ and sensitized TiO$_2$ samples

3

4   Thermogravimetric analysis (TGA) of sensitized TiO$_2$ samples and TiO$_2$-APTS material

5   (Fig. S5), further proved the incorporation of organic compounds. All curves showed a

6   small weight loss that occurs from 25 $^\circ$C to 100 $^\circ$C which can be attributed to

7   physisorbed water. TGA analysis of **TiO$_2$-3$_{COOH}$** revealed a weight loss percentage of 9.2

8   % occurring above 410 $^\circ$C due to the decomposition of the organic compound. In the

9   case of the TGA curve of TiO$_2$-APTS weight loss was observed on heating in the range

10   270 and 350 $^\circ$C and an exothermal peak at 468 $^\circ$C corresponding to the decomposition

11   of grafted aminopropyl groups (weight loss of 6.57 % or 0.34 mmolN/g). This result was

12   also checked by elemental analysis through the nitrogen content in the sample resulting

13   a similar value of 0.36 mmolN/g. In the TGA curve of **TiO$_2$-APTS-3$_{CHO}$,** the thermal

14   degradation of covalently attached organosilane ligand was observed from 300 $^\circ$C to

15   500 $^\circ$C, which corresponds to residue mass of 10.3 %. Taking into account the ligand

16   content and the surface area BET, average surface density and intermolecular distance

17   values were also calculated [31]. The sensitized samples showed similar values for these

18   parameters, 1.56 and 1.51 molec/nm^2, and 0.80 and 0.81 nm, for **TiO$_2$-3$_{COOH}$** and **TiO$_2$-**

19   **APTS-3$_{CHO}$**, respectively.

1

Table 1. Textural properties and band gap values of TiO_2 samples

| Material	S_{BET} (m².g⁻¹)	V_p^a (cm³.g⁻¹)	D_p^a (nm)	Organic content (%)[b]	Ligand content (mmol/g)[b]	Surface density (molecules/nm²)	Intermolecular distance (nm)	Particle size (nm)[c]
TiO_2	100	0.21	8.7	-	-	-	-	7.58
TiO_2-3$_{COOH}$	68.3	0.13	7.3	9.2	0.18	1.56	0.80	7.74
TiO_2-APTS-3$_{CHO}$	63.8	0.15	7.1	10.3	0.16	1.51	0.81	7.80

3   [a] Pore size and pore volume as determined by the BJH method from the adsorption of the nitrogen

4   isotherm

5   [b] Organic content determined by TGA

6   [c] Determined by Scherrer's equation

7

8   FT-IR spectra of the tris(styryl)benzene derivatives and the sensitized samples are

9   displayed in Fig. 3 and Fig. S6. In the FT-IR spectra of TiO_2 samples a broad band

10   appeared between 950-400 cm⁻¹ due to Ti-O and Ti-O-Ti bonds. Also, an additional broad

11   band was observed around 3200 cm⁻¹ which corresponds to O-H stretching vibrations of

12   hydroxyl groups on the surface of TiO_2; the band at 1635 cm⁻¹ is associated to

13   deformation vibrations of adsorbed water molecules. The bands corresponding to

14   benzene rings were observed at 1600 and 1500 cm⁻¹ and, as well as at around 1600 cm⁻

15   ¹ appeared the vibration frequency of the C=C double bonds joining the aromatic rings

16   (Fig. S6). In the FT-IR spectrum of **TiO_2-3$_{COOH}$** (Fig. 3a and S6a), the C=O stretching band

17   appeared at 1688 cm⁻¹, resulting in a similar position compared with the spectrum of

18   the **3$_{COOH}$** compound. Also, a new band was observed at 1386 cm⁻¹, characteristic of

19   symmetric stretching vibrations of carboxylate anions. These observations suggest that

20   not all carboxyl groups of the **3$_{COOH}$** were bonded to the TiO_2 surface and some carboxyl

21   groups were linked with the surface of TiO_2 through bidentate chelation. In the case of

22   FT-IR spectrum of **TiO_2-APTS-3$_{CHO}$** (Fig. 3b and S6b), the C=O band of the aldehyde group

23   was centred at 1691 cm⁻¹, which was found in a similar position in the spectrum of **3$_{CHO}$**.

24   Also, in the case of **TiO_2-APTS-3$_{CHO}$** some aldehyde groups remained free after the

25   sensitization process.
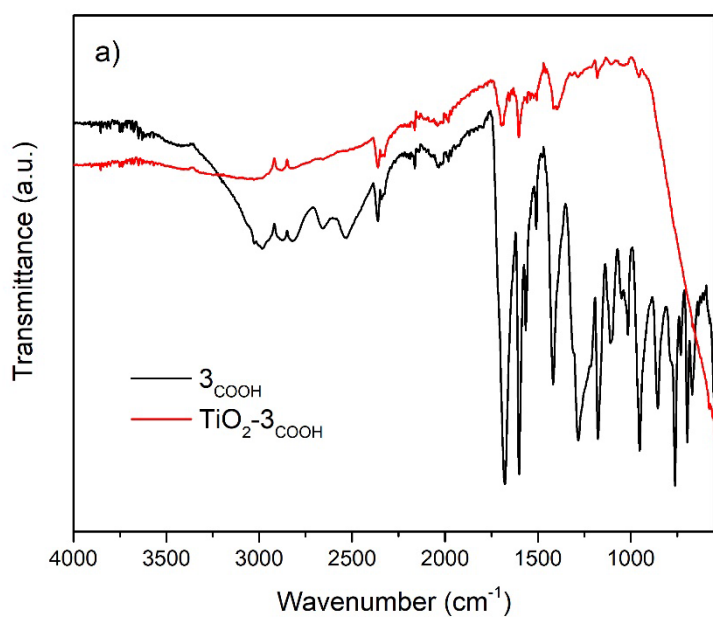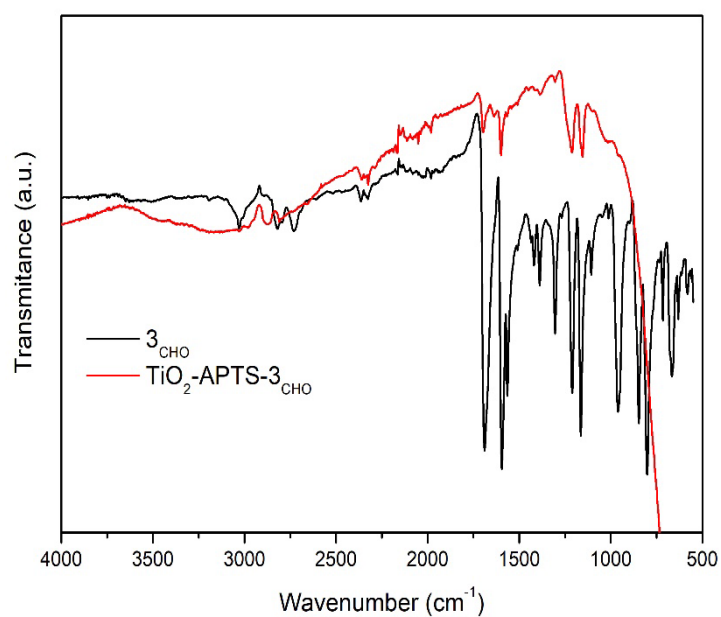
Fig. 3. FTIR spectra of a) 3_{COOH} compound and TiO_2-3_{COOH} material and b) 3_{CHO} compound and TiO_2-APTS-3_{CHO} material.

Solid-state ^{13}C NMR analysis confirmed that the TSB derivatives were attached to TiO_2 nanoparticles. The ^{13}C CP-MAS NMR spectrum of TiO_2-APTS-3_{CHO} (Fig. 4) displays signals at 9, 20 and 41 ppm attributed to the carbon atoms of the propyl alkyl chain -Si-CH_2-, -CH_2-CH_2-CH_2- and -CH_2-CH_2-CH_2-N, respectively. The signals of unreacted ethoxy

groups bonded to the Si atoms were observed at 16 and 55 ppm, which corresponding to the methyl and methylene groups, respectively. Peaks from the TSB system were located as two broad signals centred at 126 and 135 ppm. The signal at 160 ppm confirmed the formation of imine bond by reaction between the amino group of silane ligand and the aldehyde group of **3$_{CHO}$** compound. Also, the peak at 190 ppm belonged to the free aldehyde groups of **3$_{CHO}$** [24], which indicated the presence of unboned aldehyde groups in the **TiO$_2$-APTS-3$_{CHO}$** material, confirming the result obtained in the FT-IR study. In the spectrum of **TiO2-APTS-3$_{COOH}$** also appeared the signals due to TSB system at 128 and 136 ppm. The resonance peaks observed at 170 and 165 ppm corresponding to carbonyl groups of free carboxylic and attached carboxylic groups to the surface of TiO$_2$, respectively.
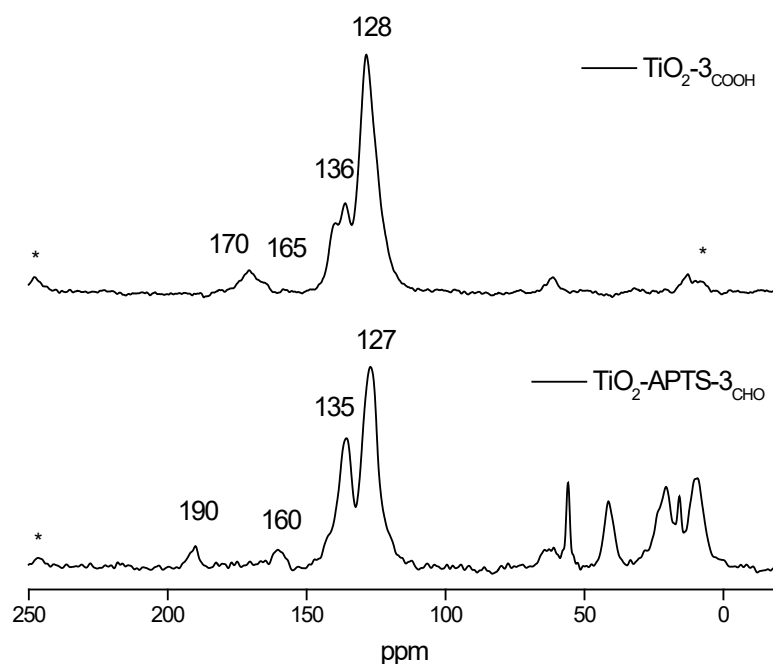
Fig. 4. ^{13}C CP-MAS NMR spectra of sensitized TiO$_2$ samples (*side bands)

In an attempt to understand the attachment between TSB molecules and the TiO$_2$ nanoparticles, a photophysical and theoretical study was conducted. UV-Vis absorption experiments in transmittance (UV-Vis) and diffuse reflectance (DRUV-Vis) were performed together with electrochemical measurements, excitation, emission spectra and quantum yields. Water was used as solvent for all synthesized compounds when the experiment requires a solution.

Free compounds (3_{COOH} and 3_{CHO}) exhibited high absorptivity in the UV range of the spectra and blue-light fluorescent behaviour (Fig. 5 and Table 2) with quantum yield values of 9% and 3%, respectively. The shape of the emission bands are wide and lack vibrionic structure which indicates that they come from different levels of energy and the blue colour of the fluorescence is consistent with a less effective conjugation of the meta-arrangement of the stilbene branches. We have previously observed that polarity of the solvent such water resulted in a dramatic decay of the quantum yield of this kind of conjugated molecules [32]. UV-Vis of **TiO₂-3$_{COOH}$** and **TiO₂-APTS-3$_{CHO}$** nanoparticles in aqueous solution presented a monotonically increasing absorbance toward higher energy as result from scattered light of the titanium nanoparticles. A predominant band in the UV range around 300 nm was observed in both cases with a high molar absorption coefficient comparable with the precursor sensitizing compounds, which indicated the presence of them in the new materials. This high molar absorption suggested a great capacity to capture the energy of light in this wavelength range. **TiO₂-3$_{COOH}$** and **TiO₂-APTS-3$_{CHO}$** nanoparticles also showed blue-light fluorescence. If these emission spectra are compared with the corresponding free dyes, there is a perfect match between **3$_{COOH}$** and **TiO₂-3$_{COOH}$** with the maximum fluorescence centered at 424 nm. However, the difference observed between **3$_{CHO}$** and **TiO₂-APTS-3$_{CHO}$** in the maximum emission may be due to the fact that the anchoring to TiO₂ implies a change in the functional group from formyl to imine which could suggest a change in the shape and shift of the fluorescence band. But the most remarkable aspect in both cases is the dramatic drop in quantum fluorescence performance when switching from TSB molecules to TiO₂ structures, indicating that non-radiative deactivation process happened on the excited state.

Table 2. Absorption maximum wavelength (λ_{ab}^{max}), molar absorption coefficient (ε), emission maximum wavelength (λ_{em}^{max}), and quantum yield (Φ_F) measured in this work for **3$_{COOH}$** and **3$_{CHO}$** compounds and **TiO₂-3$_{COOH}$** and **TiO₂-APTS-3$_{CHO}$** nanoparticles in water.

Comp.	λ_{ab}^{max} (nm) (log ε)	λ_{em}^{max} (nm)	Φ_F
3$_{COOH}$	323 (4.87)	397 (sh), 424	0.09
3$_{CHO}$	264 (5.24), 336 (4.74)	525	0.03
TiO₂-3$_{COOH}$	302 (6.16[a])	424	0.04
TiO₂-APTS-3$_{CHO}$	307 (5.54[a])	476	0.01

3

4
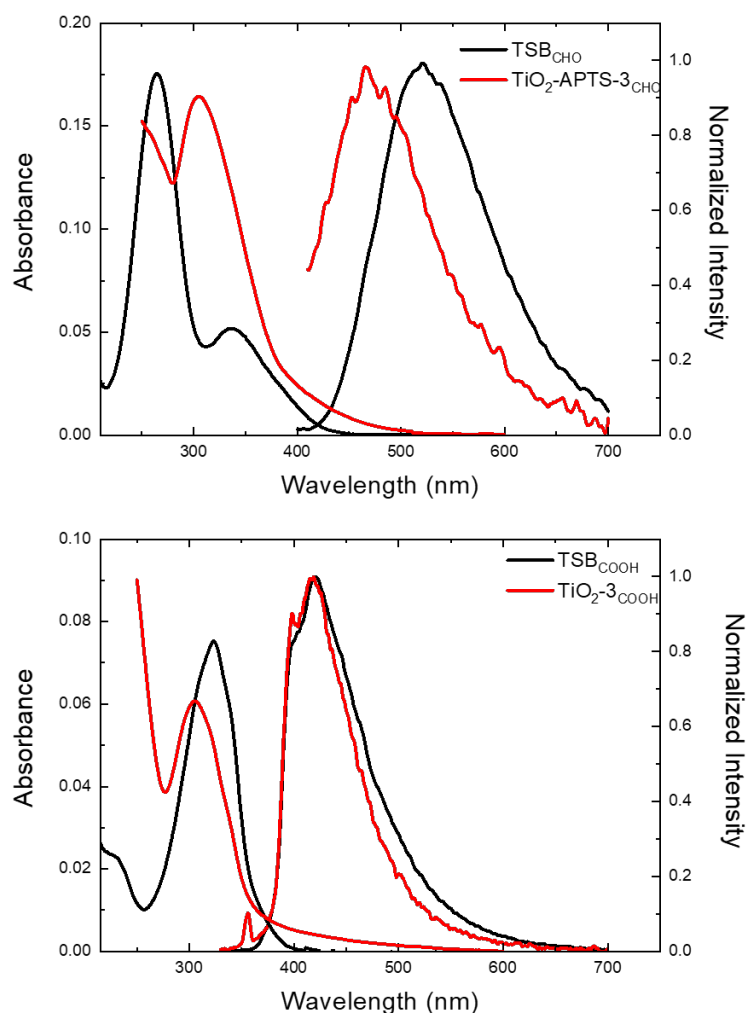
Fig. 5. UV-Vis and fluorescence spectra of **3$_{CHO}$** (1μM) and **TiO$_2$-APTS-3$_{CHO}$** (4·10^{-1} μM) on top

and **3$_{COOH}$** (1μM) and **TiO₂-3$_{COOH}$** (4·10^{-2} μM) on bottom in water.

7

8   The DRUV-Vis spectra of bare and functionalized TiO₂ samples revealed that the TiO₂

9   nanoparticles had been sensitized by TSB derivatives (Fig. 6). The spectrum of TiO₂

10   exhibited characteristic absorption bands in the UV region corresponding to the anatase

11   phase. In the spectra of both modified TiO₂ samples, the band absorption was shifted to

12   visible region (above 400 cm^{-1}) compared to that of bare TiO₂ which was indicative that

13   the surface modification of TiO₂ with the TSB compounds changed the behaviour of TiO₂

14   nanoparticles into a visible light absorptive material. The band gap values were

15

1   calculated by the application of the Kubelka-Munk algorithm (Fig. S7). The band gap was

2   further decreased after the organic functionalization resulting in a value of 3.14 eV for

3   the unmodified TiO_2 sample, while **TiO_2-3$_{COOH}$** and **TiO_2-APTS-3$_{CHO}$** possess band gaps of

4   2.57 and 2.69 eV, respectively (Table 3). These results confirmed the successful

5   sensitization process on TiO_2 nanoparticles.
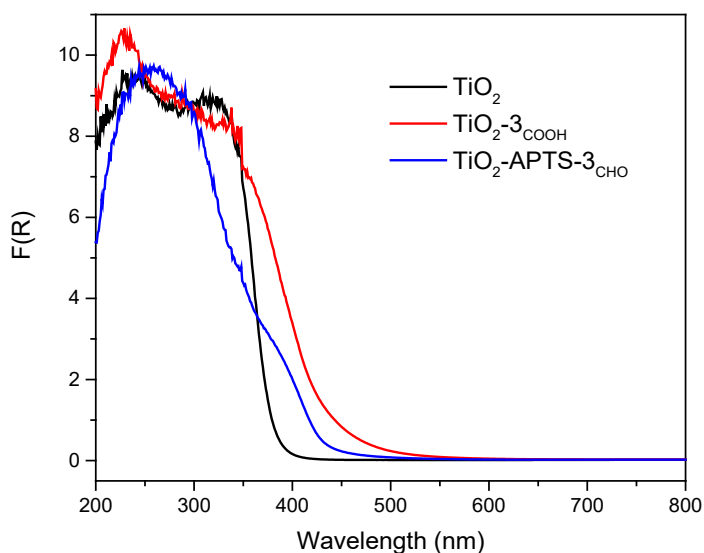
Fig. 6. DRUV-Vis spectra of TiO_2 and sensitized samples.

9   Electrochemical measurements were performed for bare, dye-sensitized TiO_2

10   samples and TSB compounds to experimentally estimate their E_{HOMO} and E_{LUMO} values.

11   The HOMO and LUMO energy levels were from the following equations:

12 $$E_{LUMO} = -(E_{red} + 4.8) \text{ eV}$$

13 $$E_{HOMO} = -(E_{ox} + 4.8) \text{ eV}$$

14 $$E_{HOMO} = E_{LUMO} - E_g$$

15   Where E_{red} and E_{ox} are onset reduction and oxidation potentials versus the ferrocene

16   electrode and E_g is the optical band gap of the samples. E_g can be calculated by the

17   equation of $E_g = 1240/\lambda_g$ (where λ_g is the absorption edge of the material) (see Fig. 6).

18   On the basis of the electrochemical data, E_{HOMO} and E_{LUMO} were estimated to be -6.67

19   and -3.91 eV, and -6.57 and -3.82 eV, for **TiO_2-3$_{COOH}$** and **TiO_2-APTS-3$_{CHO}$**, respectively

20   (see Fig. S8) (Table 3). For comparison purposes, the energy levels were also calculated

1   for non-modified TiO_2 and the obtained results are in agreement with previous

2   published studies [33-35] .

3

4   **Table 3.** Band gap values and electrochemical data of samples.

| Material	Band gap (eV)	E_{LUMO} (eV)	E_{HOMO} (eV)	E_g (eV)
TiO_2	3.14	-3.85	-7.07	3.22
3_{COOH}	2.56	-3.22	-5.88	2.66
3_{CHO}	2.70	-3.59	-6.22	2.63
TiO_2-3_{COOH}	2.57	-3.91	-6.67	2.76
TiO_2-APTS-3_{CHO}	2.69	-3.82	-6.57	2.75

5

6

7   **3.2. Computational studies**

8   In order to try to clarify the type of interaction between the TSB molecules and TiO_2,

9   computational studies were carried out and electronic structures and optical properties

10 were calculated for 3_{COOH} and 3_{CHO} and for their respective TiO_2 materials. Two

11 functionals were employed for these calculations, M06-2X and B3LYP. M06-2X was

12 chosen because of its higher percentage of HF exchange (54%) when compared to

13 methods such as B3LYP (20%), which helps reducing the overestimation of the electron

14 delocalization and shows an adequate behaviour in the calculation of molecular

15 geometries of conjugated systems [36, 37]. B3LYP functional was chosen as it is one of

16 the most employed functionals when running DFT calculations because of its reduced

17 number of parameters and its overall good results. In addition, it provides excellent

18 linear relationships between the calculated energies of HOMO and LUMO orbitals and

19 the experimental ionization potentials and electron affinities [38], thus making it an

20 optimal choice for the estimation of E_g. All input structures were subjected to energy

21 minimization in water as solvent, followed by simulation of the absorption spectra for

22 each compound through a time-dependent DFT (TD-DFT) calculation in water, as it was

23 the solvent employed in the electrochemistry, UV-Vis and fluorescence experiments as

24 well as for the evaluation of the photocatalytic degradation properties. Initially, the

25 energies of the two possible conformers for 3_{COOH} and 3_{CHO} were calculated, which

26 yielded an energy difference of 0.444 and 0.479 kcal/mol, respectively. As this difference

was found to be extremely small, the computational calculations were conducted for only one of the conformers of each molecule (Fig. S9). As we have previously observed for this kind of molecules, 3_{COOH} and 3_{CHO} have a rigid and π-conjugated structure where the styryl branches are slight twisted by way of propeller [35].

Binding to the titanium oxide surface was modelled in the case of the aldehyde as an APTS-imine with a SiO_2-TiO_2 cluster at the end of the propyl chain. Due to the flexibility of the propyl chain, 3_{CHO} could bind via two aldehyde moieties, so both complexes, with one (**1APTS**) and two APTS (**2APTS**) molecules were studied (Fig. S10).

Optimized structures by M06-2X showed a more twisted geometry than those resulting from B3LYP, a reasonable result taking into account the aforementioned reduction in electron delocalization overestimation caused by the inclusion of a higher percentage of HF exchange energy. In any case, the results were consistent and comparable with those found for 3_{CHO}.

M06-2X energies of the HOMO and LUMO for all orbitals of **TiO_2-APTS-3_{CHO}** remained essentially unchanged with respect to 3_{CHO}. Geometry of the HOMO-LUMO orbitals showed that the electronic density in the 3_{CHO} molecule was shifted from being more concentrated in a single arm of the compound (HOMO) to being focused on the other two arms (LUMO), as was the case for **TiO_2-APTS-3_{CHO} (1 APTS)** although more pronounced in the latter. HOMO orbital of **TiO_2-APTS-3_{CHO} (2 APTS)** was centred on the TSB arms bound to the two APTS linkers, while the LUMO orbital had its electronic density centred on the remaining arm of the compound (Fig. 7a).
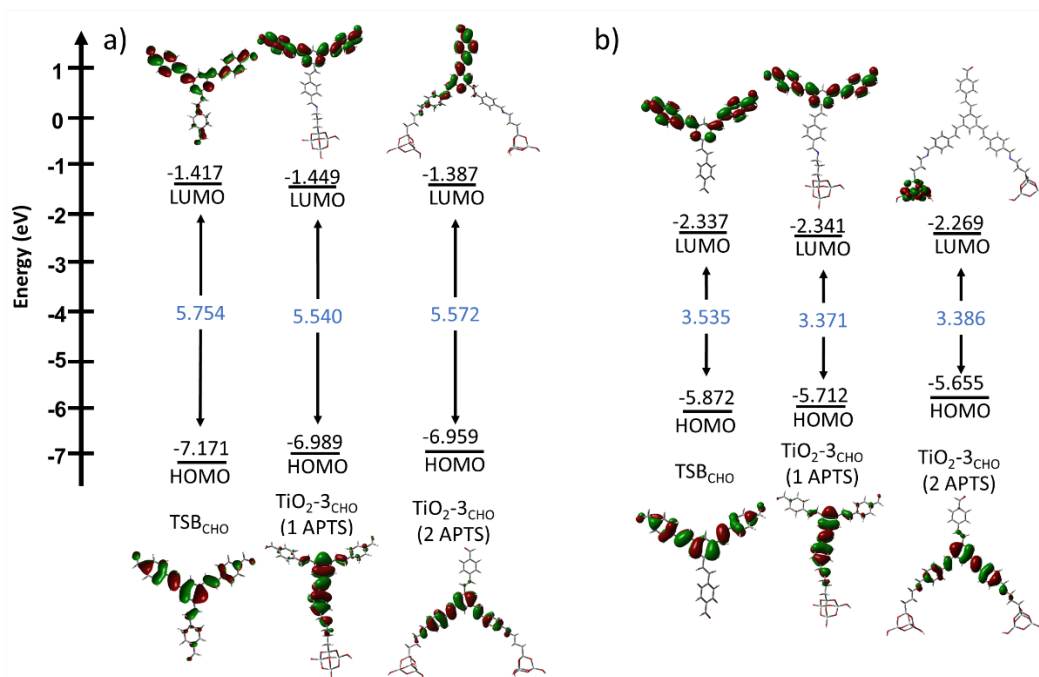
Fig. 7. Energy levels diagram for HOMO and LUMO orbitals and calculated values of E_g for aldehyde-based materials calculated at a) M06-2X/6-31G* and b) B3LYP/6-31G* levels of theory.

B3LYP orbital geometries were comparable for **3$_{CHO}$** and **TiO$_2$-APTS-3$_{CHO}$ (1 APTS)** with M06-2X. However, the most unexpected result was the fact that in **TiO$_2$-APTS-3$_{CHO}$ (2 APTS)**, the LUMO orbital had its electronic density located exclusively on one of the TiO$_2$ clusters. Apparently, this finding would suggest that excitation of the electron may involve titanium orbitals in opposite results from M06-2X calculations. In order to explain this issue, vertical transitions were calculated for all structures through both methods. Results are summarized in Table S2. Values of HOMO, LUMO and E_g obtained with B3LYP functional were closer to the experimental values (Table 3) than those of M06-2X, as it has been explained in previous paragraphs and demonstrated for this type of molecules [28].

Calculated absorptions at TD-M06-2X level for **3$_{CHO}$** were located at 319.07 nm (f=1.9662, assigned to the S$_0\rightarrow$S$_4$ transition) and 317.45 nm (f=1.9668, assigned to S$_0\rightarrow$S$_5$). Both transitions were assigned to the experimental absorption maximum located at 336 nm, and the components for each of them involved similarly contributing transits between HOMO-2, HOMO-1 and HOMO to LUMO, LUMO+1 and LUMO+2. **TiO$_2$-APTS-3$_{CHO}$ (1 APTS)** presented two absorptions with high oscillator strength: S$_0\rightarrow$S$_3$ at 325.87 nm (f=1.4622) and S$_0\rightarrow$S$_4$ at 320.57 nm (f=2.0277). The main contribution in the

19

first one was HOMO→LUMO (33% contribution), while the contributions for the second absorption were evenly spread across different components. Transitions for **TiO$_2$-APTS-3$_{CHO}$ (2 APTS)** were computed at 323.23 nm (f=1.5098, S$_0$→S$_3$) and at 320.57 nm (f=2.2180, S$_0$→S$_4$). For the first one, the most important contribution was HOMO→LUMO (45% contribution), while for the second absorption it was HOMO-1 LUMO (44%). Both transitions were assigned to the experimental absorption maximum located at 307 nm. In both cases, **TiO$_2$-APTS-3$_{CHO}$ (1 APTS)** and **TiO$_2$-APTS-3$_{CHO}$ (2 APTS),** the transitions happen just among TSB orbitals and titanium orbitals are never involved (see orbital structures in Fig. S12). The only computed orbitals that had electronic density in the titanium clusters were involved in transitions with very low probability of occurring (HOMO+8 and LUMO+13 for **TiO$_2$-APTS-3$_{CHO}$ (1 APTS)** (Fig. S13), and LUMO+17 and LUMO+21 for **TiO$_2$-APTS-3$_{CHO}$ (2 APTS)** (Fig. S15), respectively). Therefore, no direct transference of electrons from the dye to the nanoparticle could be expected. However, the difference in energy between some of these levels might be low enough to allow for the secondary transference of an excited electron from the recipient LUMO to one of these orbitals with electronic density in the TiO$_2$ cluster, a process that would imply a Type I sensitization mechanism.

Computed transitions and experimental UV spectra for all materials are overlaid in Fig. S29. The theoretical transitions are comprised within the band envelope indicating a good agreement between computational and experimental values.

Upon conducting the TD-B3LYP calculations on these compounds, we were presented with a much higher number of transitions that composed the theoretical UV spectra in comparison with the results from TD-M06-2X. **3$_{CHO}$** presented several absorptions, with the main ones located at 372.97 nm (f=1.2254, assigned to the S$_0$→S$_2$ transition) and 372.33 nm (f=1.1487, assigned to S$_0$→S$_3$). The spectrum maximum was located at 364.85 nm, which was 29 nm higher than the experimental value of 336 nm. **TiO$_2$-APTS-3$_{CHO}$ (1 APTS)** presented several low intensity absorptions, with the most intense ones being located at 353.21 nm (S$_0$→S$_{10}$, f=0.8352), 382.04 nm (S$_0$→S$_5,$ f=1.1218) and 391.16 nm (S$_0$→S$_2,$ f=0.6799). Predicted UV spectrum had a single maximum at 371.65 nm, very far away from the experimental value of 307 nm, which established M06-2X as the functional of choice to predict the optical activity of these compounds. Components of the S$_0$→S$_2$ absorption were HOMO→LUMO (63 %) and

HOMO→LUMO+3 (29 %). The most important component present in the S_0→S_5 transition was HOMO-1→LUMO+3, with a 90 % contribution, while S_0→S_{10} transition was mainly contributed by HOMO-2→LUMO (35%), HOMO-1→LUMO+5 (21%) and HOMO→LUMO+5 (26 %). All these orbitals exhibited electronic density only on the **3_CHO** molecule, with no involvement of titanium-centered orbitals (Fig. S12). Only two weak absorptions, one located at 348.69 nm (S_0→S_{11}, f=0.3084), and the other one at 348.38 nm (S_0→S_{12}, f=0.0122) had components that involved a direct transition to orbital LUMO+4, which had its electronic density located only at the titanium cluster. As before, orbitals containing electron density in the metal centers were involved in low probability transitions (LUMO+2 and LUMO+4 for **TiO₂-APTS-3_CHO (1 APTS)** (Fig. S23), and LUMO+1 and LUMO+2 for **TiO₂-APTS-3_CHO (2 APTS)** (Fig. S25), respectively), accounting for the same type of photosensitization mechanism obtained from M06-2X.

TiO₂-APTS-3_CHO (2 APTS) too, presented several low intensity absorptions, being the most intense the ones located at 363.14 nm (S_0→S_{12}, f=0.5027), 372.17 nm (S_0→S_{10}, f=1.0631) and 391.40 nm (S_0→S_2, f=0.879). Predicted UV spectrum had one maximum at 377.92 nm, close to the value of the **TiO₂-APTS-3_CHO (1 APTS)** and also far away from the experimental value of 307 nm. Components of the S_0→S_2 absorption were HOMO-1→LUMO+1 (67 %). The most important components of the S_0→S_{10} transition were HOMO-1→LUMO+7 (56 %) and HOMO→LUMO+7 (26 %). In S_0→S_{12} transition, the main contributor was HOMO→LUMO+8 (90 %). No contribution of LUMO is observed for the main transition indicating that although this LUMO orbital is participating by the titanium does not participate in the absorption of light and electron excitation process. Parallel, all the orbitals involved in the transitions had the electronic density located on the TSB chromophore part of the nanomaterial. Experimental UV spectra for all materials are overlaid with the respective calculated transitions in Fig. S30.

From this theoretical analysis, several conclusions were extracted. The first one was that M06-2X results predicted UV spectra much better than B3LYP although the latter predicted better, the E_g gap for all materials studied. Regardless of the calculation method employed, results from both TD-DFT calculations agreed that electron transition during the absorption process just involve electrons in orbitals from the dye and no electron density on the TiO_2 cluster. Moreover, the energy of LUMO orbitals where the titanium clusters contributed but had no involvement in the electronic transitions, were

found to have energies close to the corresponding LUMO orbitals of the TSB, suggesting that sensitization would take place through an energy transfer process in a Type I mechanism of photosensitization of the TiO_2 nanoparticle.

A similar analysis to the previous one was conducted for the carboxylic acid materials. In this case, compound **TiO_2-3$_{COOH}$** was different, since the carboxylic acid moieties were bonded directly to the TiO_2 surface. The initial challenge was to elucidate which of the possible modes of carboxylate binding was occurring. According to literature [6] three possibilities were considered: type A, where one titanium atom forms an ester with the carboxylate in monodentate way (bound to one oxygen atom). Another one (type B), where a single titanium atom binds to both oxygens of the carboxylate group (thus forming a bidentate chelate), and finally, type C, where each oxygen in the carboxylate would bind one Ti atom in a more complex cluster (Scheme 1).
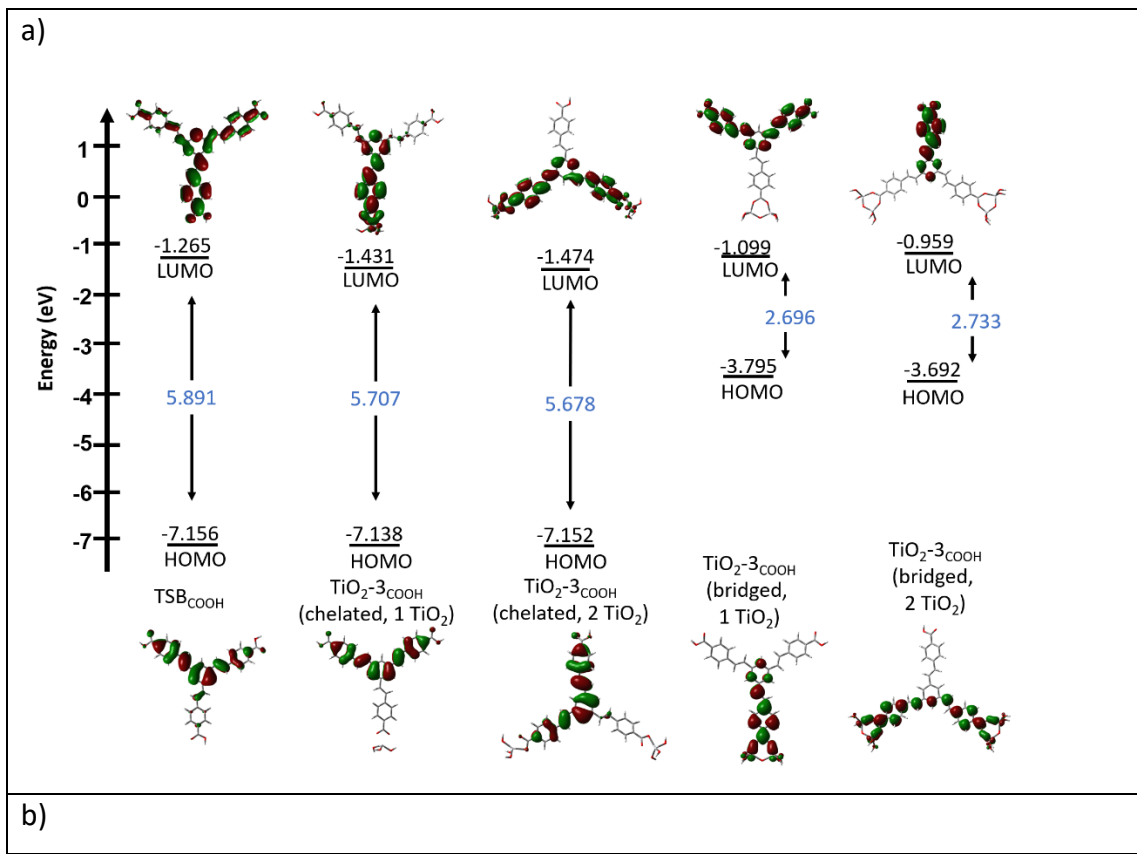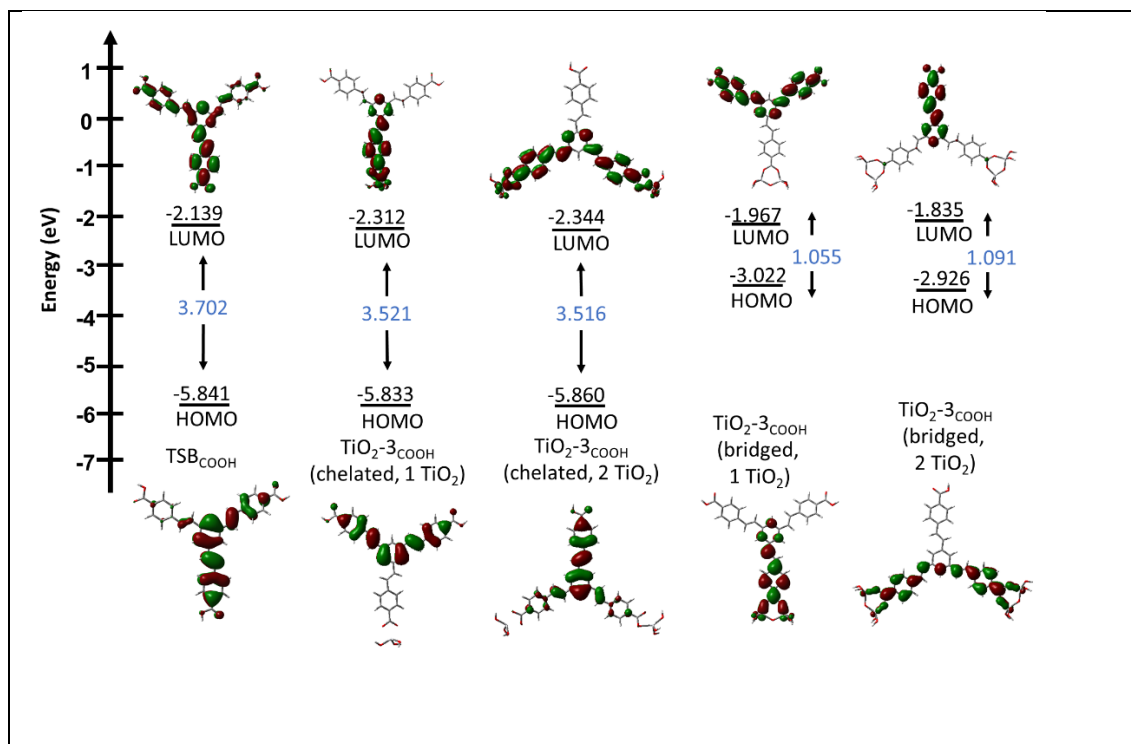

Type A   **Type B**   **Type C**
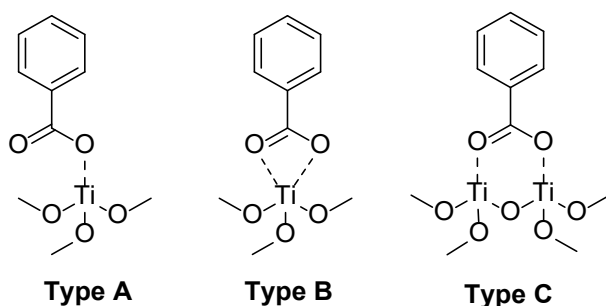
Scheme 1. Different anchoring modes for carboxylic acid groups to TiO_2 surface.

The first two modes were modelled starting from the same monodentate ester depicted in type A, between the carboxylic acid and a $Ti(OH)_3$ cluster (Fig. S31), while bidentate bridge from type C complex was built by binding each oxygen of the carboxylate to the titanium atoms of a $Ti_2(O)(OH)_4$ cluster (Scheme 1). For each of the described structures, the attachment of the molecules to the TiO_2 surface was modelled for one and two anchoring points (example in Fig. S31d).

After conducting geometry optimizations with M06-2X and B3LYP functionals, the most evident result was that the initial monodentate esters Type A complexes evolved into Type B bidentate chelates in all structures and the increase in the HOMO energy in Type C results in values of the HOMO-LUMO gap three-fold lower than expected. Therefore, the anchoring way of TSB over the surface of the TiO_2 is better described as Type B. (Fig. 8).

1

2

3

4

5

6

7

8

9

10

11

a)

Energy (eV)

-1.265
LUMO

-1.431
LUMO

-1.474
LUMO

-1.099
LUMO

-0.959
LUMO

5.891

5.707

5.678

2.696

2.733

-3.795
HOMO

-3.692
HOMO

-7.156
HOMO

-7.138
HOMO

-7.152
HOMO

TSB$_{COOH}$

TiO$_2$-3$_{COOH}$
(chelated, 1 TiO$_2$)

TiO$_2$-3$_{COOH}$
(chelated, 2 TiO$_2$)

TiO$_2$-3$_{COOH}$
(bridged,
1 TiO$_2$)

TiO$_2$-3$_{COOH}$
(bridged,
2 TiO$_2$)

b)

Fig. 8. Energy level diagram and Eg values for the HOMO-LUMO orbitals of all carboxylic acid compounds studied through DFT at a) M06-2X/6-31G* and b) B3LYP/6-31G* level.

A previously encountered, HOMO, LUMO and Eg values obtained from B3LYP calculations were closer to the experimental results (Table 3) than M06-2X, and although computational studies helped us to point out that type B complex is what better represent the anchoring between TSB and TiO_2, we could not differentiate between binding to the surface through one carboxylate or two carboxylates groups, as the E_g values were too similar between them. On the other hand, if the optimized geometry of the complex formed is analyzed and the rigidity of the conjugate molecule considered, the arrangement of the TSB molecule must be perpendicular to the surface of the TiO_2 nanoparticle which forces the orientation of at least one of the carboxylic acid groups of the TSB towards the medium, which is in agreement with the results mentioned above in solid-state ^{13}C NMR analysis for **TiO₂-3COOH.**

TD-DFT analysis of **TiO₂-3COOH** material was performed at M06-2X and B3LYP levels of theory with 6-31G* basis set. The results of these calculations are shown in Table S3. Electronic transitions calculated for the **3COOH** showed two intense transitions: one located at 311.2 nm (f=1.9881) and assigned to the $S_0{\rightarrow}S_1$ transition with several

contributions. The other one was calculated at 309.7 nm (f=1.9563), which was assigned to $S_0{\rightarrow}S_2$; within this absorption, the main contribution for this transition was HOMO→LUMO (27%). In general, the experimental and calculated absorption maximum for **TiO$_2$-3$_{COOH}$** agree considering the bandwidth of the UV-vis spectra. **TiO$_2$-3$_{COOH}$ (2 TiO$_2$)** experienced a slight bathochromic shift in the energy of the transitions compared to that bound to just one Ti atom (Fig. S32a-b). For the case of type C structures, calculated transitions appeared at much longer wavelengths (530-650 nm) than the experimental values, confirming the results from the Eg calculation and ruling out this mode of binding to the TiO$_2$ nanoparticle. Therefore, these structures were not further considered (Fig. S32c-d). Both $S_0{\rightarrow}S_1$ and $S_0{\rightarrow}S_2$ transitions were assigned to the experimental absorption maximum located at 323.6 nm.

TiO$_2$-3$_{COOH}$ (1 TiO$_2$) presented two absorptions, with high oscillator strength: $S_0{\rightarrow}S_1$ at 319.38 nm (f=2.1248) and $S_0{\rightarrow}S_2$ at 313.30 nm (f=1.9006). The main contribution in the first one was HOMO-1→LUMO (49 % contribution), while the second absorption was mainly contributed by HOMO→LUMO+2 (37 %). **TiO$_2$-3$_{COOH}$ (2 TiO$_2$)** exhibited two absorptions located at 323.10 nm (f=2.1745, assigned to $S_0{\rightarrow}S_1$) and at 315.92 (f=2.0667, assigned to $S_0{\rightarrow}S_2$). Components for $S_0{\rightarrow}S_1$ absorption were HOMO-1→LUMO+1 (34 %) and HOMO→LUMO (34%), while for $S_0{\rightarrow}S_2$ absorption were HOMO-1→LUMO (32 %).

TD-B3LYP calculations yielded less accurate UV absorption predictions: **3$_{COOH}$** presented its most intense absorptions at 372.13 nm (f=1.2966, assigned to $S_0{\rightarrow}S_2$) and at 371.89 nm (f=1.2566, assigned to $S_0{\rightarrow}S_3$). A pair of weak absorptions were also located at 327.43 nm and at 327.07 nm, but oscillator strengths were lower than 0.5. Main contributions to the $S_0{\rightarrow}S_2$ absorption were HOMO-1→LUMO+1 (35 %) and HOMO→LUMO (37 %). **TiO$_2$-3$_{COOH}$ (1 TiO$_2$)** presented several absorptions being that with the highest oscillator strength the one located at 387.11 nm (f=1.4113, assigned to $S_0{\rightarrow}S_2$). Two weaker absorptions were located at 374.52 nm (f=0.7555, assigned to $S_0{\rightarrow}S_3$) and at 359.10 nm (f=0.7896, assigned to $S_0{\rightarrow}S_4$). For the $S_0{\rightarrow}S_2$ absorption, the most important component was HOMO-1→LUMO (78%). For $S_0{\rightarrow}S_3$, the main component was HOMO-1→LUMO+1 (78 %) and for $S_0{\rightarrow}S_4$ it was HOMO→LUMO+2 (92 %). **TiO$_2$-3$_{COOH}$ (2 TiO$_2$)** calculated absorptions consisted of one located at 390.27 nm (f=1.5492, assigned to $S_0{\rightarrow}S_2$) together with a weaker absorption that appeared at 383.86 nm (f=0.8614, assigned to $S_0{\rightarrow}S_3$) (Fig. S20c and S20d). Other transitions with

oscillator strength lower than 0.5 appeared at 373.11, 350.09 and 339.87 nm, but were not considered for the study. For the $S_0 \rightarrow S_2$ absorption, the most important component was HOMO-1$\rightarrow$LUMO+1 (79 %). For $S_0 \rightarrow S_3$, the main component was HOMO-1$\rightarrow$LUMO (61 %). Similarly to the case of the aldehyde materials, TD-B3LYP yielded worse accuracy in the prediction of the UV spectra of the studied compounds but better prediction on E_g values. However, both TD-B3LYP and TD-M06-2X geometries were almost identical for all orbitals relevant to light absorption: HOMO orbitals were contributed mostly by the dye, while the LUMOs were a combination of orbitals from the dye and the TiO_2 nanoparticles, thus accounting for a direct electronic injection of the electron and suggest a Type II mechanism of sensitization of the TiO_2 nanoparticles.

As a summary from the theoretical calculations, **TiO_2-APTS-3$_{CHO}$** material was found to be sensitized through light absorption, followed by excitation of the dye and transference of the energy to the TiO_2 nanoparticle in a Type I mechanism of sensitization; **TiO_2-3$_{COOH}$** material, however, showed activation through a Type II mechanism where electrons from HOMO-type orbitals of the dye are promoted to LUMO-type orbitals focused on the TiO_2 nanoparticles resulting in a direct electronic injection.

3.3. Photocatalytic degradation of dye pollutants

The photocatalytic activity of TiO_2 samples was studied for degradation of MB and MO in aqueous solution under irradiation UV or visible lights. The zeta potential of TiO_2 samples was measured in aqueous phosphate buffer solution at pH = 7.4. The value of zeta potential of unmodified TiO_2 is -25.33, which is due to the deprotonation of hydroxyl groups of the surface. For **TiO_2-APTS-3$_{CHO}$** nanoparticles, the zeta potential value became less negative (-14.09), as excepted, due to the decrease of free hydroxyl groups by incorporation of **3$_{CHO}$** compound on aminopropyl-modified TiO_2 nanoparticles [25]. In the case of **TiO_2-3$_{COOH}$** nanoparticles also exhibited negative charge with a zeta potential value -22.19, which was similar to that of bare TiO_2, suggesting that the presence of **3$_{COOH}$** compound, with negatively charged carboxylate groups, had an influence on the surface charge. These results indicate that the negatively charged surface of TiO_2 samples can favour the adsorption of cationic pollutants as MB.

3.3.1. Photocatalytic degradation of aqueous methylene blue (MB)

The degradation of MB in aqueous solution (50 mL, 0.04 mM) was carried out using a low dosage of catalyst 0.4 g L^{-1} under irradiation UV, LED and visible lights. First, the suspensions were stirred in darkness for 1 h to achieve the adsorption – desorption equilibrium. Then, the adsorption capacities of TiO$_2$ samples were calculated by recovered UV-vis spectra of MB solution. As can be seen in Fig. 9a, the adsorption rate of MB on **TiO$_2$-3$_{COOH}$** was the highest (about 53 %) in comparison with the obtained values over bare TiO$_2$ and **TiO$_2$-APTS-3$_{CHO}$** which were 3.8 % and 15.3 %, respectively. The high MB adsorption onto **TiO$_2$-3$_{COOH}$** can be explained by electrostatic interactions between cationic MB and negatively charge carboxylate groups of **TiO$_2$-3$_{COOH}$** nanoparticles and, additionally, π stacking interactions between aromatic rings. Hence, the fact that MB presented a higher adsorption on **TiO$_2$-3$_{COOH}$** can favour the photocatalytic degradation. In general, sensitized TiO$_2$ nanoparticles exhibited higher photocatalytic activity than that obtained with bare TiO$_2$ under different irradiation sources. After UV irradiation for 60 min, only a 41.1 % of degradation was achieved by TiO$_2$ and 72.5 % and 93.3 % were obtained using **TiO$_2$-APTS-3$_{CHO}$** and **TiO$_2$-3$_{COOH}$**, respectively. LED irradiation leads to a decrease in the photocatalytic activity of TiO$_2$ (2.1 %) or **TiO$_2$-APTS-3$_{CHO}$** (20.7 %), while the great photocatalytic activity of **TiO$_2$-3$_{COOH}$** was preserved (see Fig. 9a). According to the data plotted in Fig. 9b, the photocatalytic degradations of MB for TiO$_2$ samples followed the pseudo-first-order kinetic. Comparing the results obtained using UV and LED lights, the greatest rate constant value was reached for **TiO$_2$-3$_{COOH}$** (k = 0.046 min^{-1}) under UV irradiation, while the k values obtained for **TiO$_2$-APTS-3$_{CHO}$** and unmodified TiO$_2$ were k = 0.0073 min^{-1} and k = 0.0081 min^{-1}, respectively. Nguyen et al. [39] accomplished similar reaction rate constant (k = 0.044 min^{-1}) using 1 g L^{-1} of TiO$_2$ doped with Pd and applying UV at 100 W. The results obtained by other systems reported are represented in Table 4.

Table 4. Comparing of different catalysts for photocatalytic degradation of dye pollutants

Catalyst	Light (power)	k (min^{-1})	Dye Pollutant	Catalyst load (g/L)	Time (min)	Removal (%)	Ref
TiO$_2$-3$_{COOH}$	UV (36 W)	0.046	MB	0.4	60	93.3	This work

TiO$_2$-APTS-3$_{CHO}$	UV (36 W)	0.0074	MB	0.4	60	72.5	This work
0.5%Pd-TiO$_2$	UV (100 W)	0.044	MB	1	120	99.4	[39]
Pt$_{0.8}$/TiO$_2$-WO$_3$	UV + Air	-	MB	0.2	90	98	[40]
Cr$_2$O$_3$/TiO$_2$	UV	0.0198	MB	1	60	90	[41]
TiO$_2$-3$_{COOH}$	VIS (300 W)	0.100	MB	0.4	30	98	This work
TiO$_2$-APTS-3$_{CHO}$	VIS (300 W)	0.042	MB	0.4	90	99.9	This work
Zn-porphyrins	VIS (50 W) + Air	-	MB	-	30	> 70	[11]
Pt$_{0.8}$/TiO$_2$-WO$_3$	VIS (180 W)	-	MB	0.2	90	75	[40]
TiO$_2$-3$_{COOH}$	UV (36 W)	0.0073	MO	0.4	150	70.3	This work
TiO$_2$ nanorods	UV (650 lux)	-	MO	0.5	150	51	[42]
TiO$_2$-3$_{COOH}$	VIS (300 W)	0.0097	MO	0.4	150	79.9	This work
TiO$_2$-3$_{COOH}$	VIS (300 W)	0.057	MO	1	60	98	This work
Cu-TiO$_2$/ZnO	VIS (23 W)	-	MO	1.5	120	85.5	[43]
C$_{60}$-AuNPs-TiO$_2$	Solar (500 W)	0.0203	MO	1	160	95	[44]

Fig. 9c and 9d illustrate the excellent results obtained in the degradation of MB when visible light was used. Unmodified TiO$_2$ showed low visible photocatalytic activity, as expected, with a degradation ratio of 27% in 30 min, which is similar to the value found in photolysis of MB. Nevertheless, the degradation was accomplished in 30 min with **TiO$_2$-3$_{COOH}$** photocatalyst ($k = 0.100$ min^{-1}) and with **TiO$_2$-APTS-3$_{CHO}$** completed in 90 min ($k = 0.042$ min^{-1}). Thus, **TiO$_2$-3$_{COOH}$** proved to be 6.2 times faster than the bare TiO$_2$ nanoparticles.
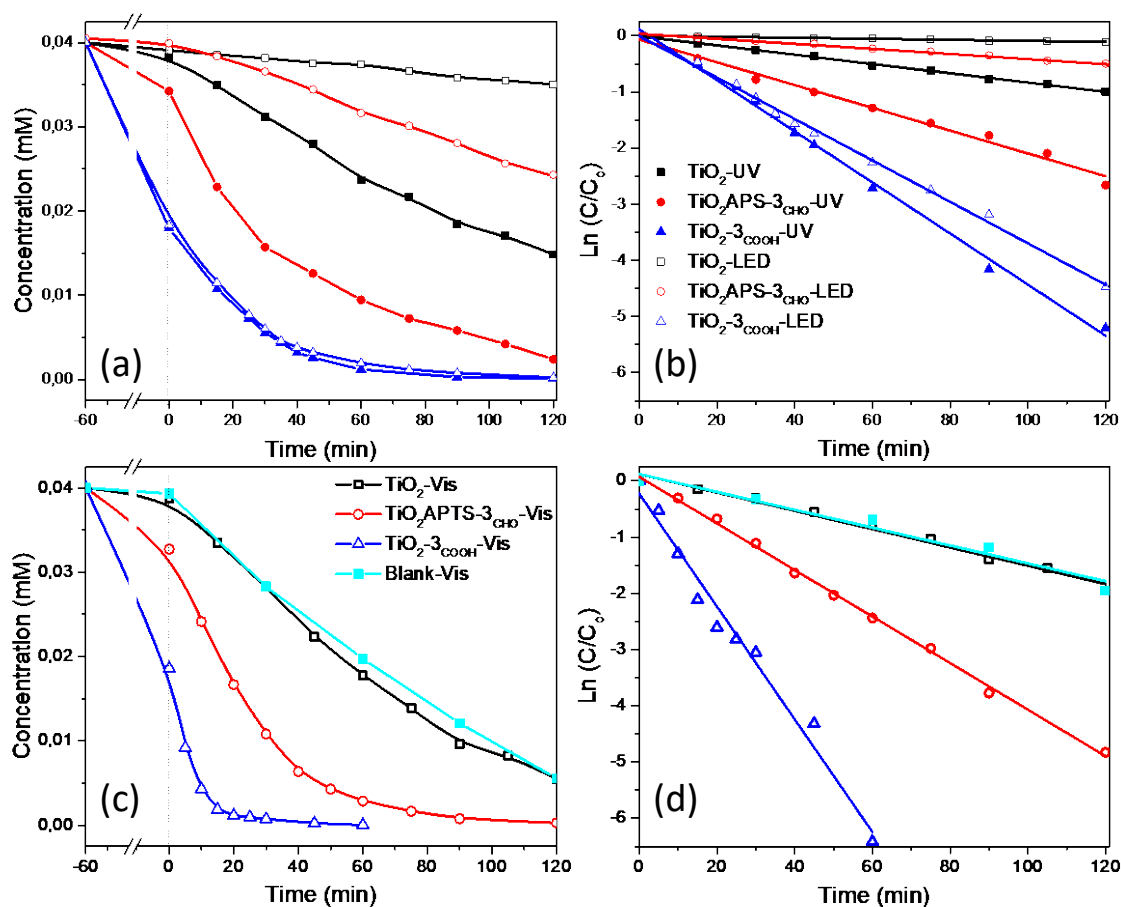
Fig. 9. Photocatalytic degradation of MB using TiO_2 samples. (a), (b) Comparison between using UV or LED lights and (c), (d) visible light.

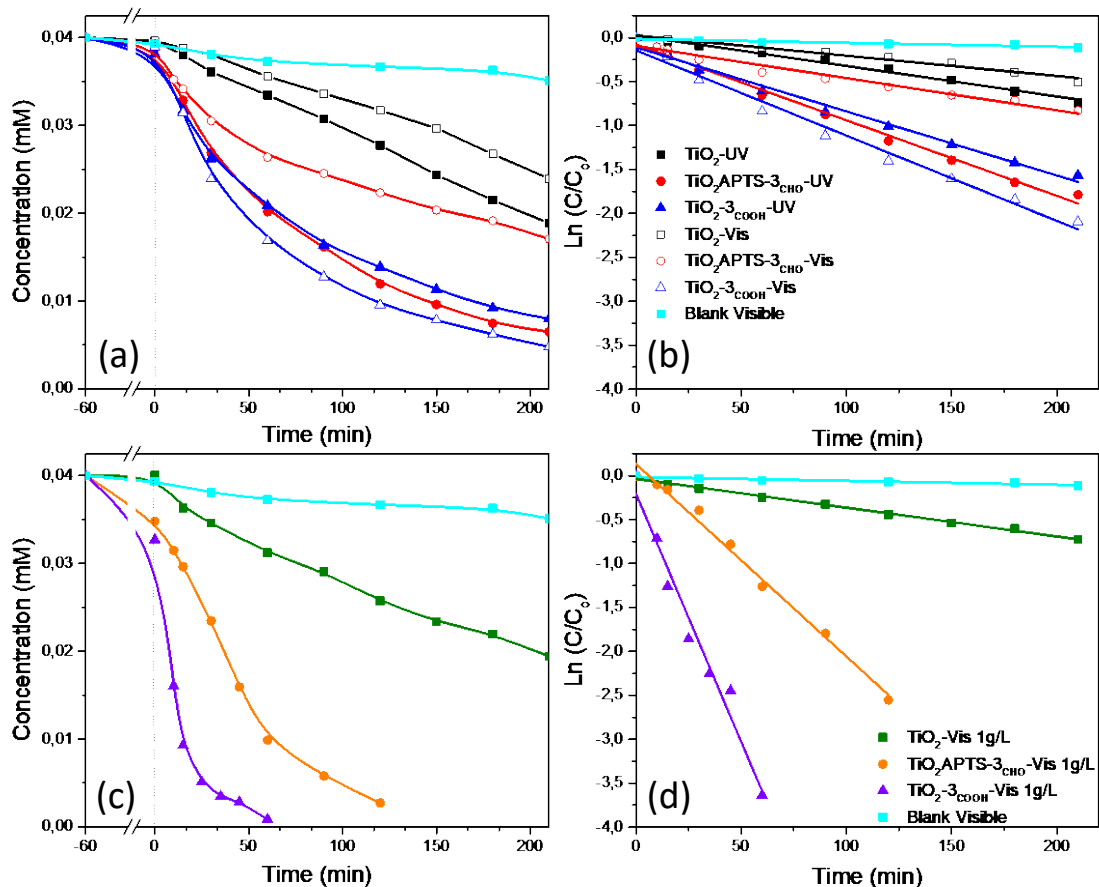### 3.3.2. Photocatalytic degradation of aqueous methyl orange (MO)

The photocatalytic performance of TiO_2 samples was also studied in the degradation of OM (50 mL, 0.04 mM of aqueous solution) with a low dosage of photocatalyst (0.4 g L^{-1}) and in presence of UV or visible light (Fig. 10a). Initially, the suspension was stirred for 1 h under dark condition to achieve adsorption and desorption equilibrium, and then the adsorption capacity examined. The adsorption rate of MO on bare TiO_2 was lower (3.8 %), while the adsorption on sensitized TiO_2 nanoparticles was slightly higher, 7.2 % of adsorption rate on **TiO₂-3_COOH** and 8.5 % in the case of **TiO₂-APTS-3_CHO**. MO is an anionic dye and this fact limits its interaction with TiO_2 samples which are negatively charged. However, sensitized TiO_2 nanoparticles could form π stacking interactions with MO since they contain π bonds. Thus, bare TiO_2 material showed low degradation efficiency (38.4 % within 150 min) under UV light, while **TiO₂-3_COOH** and **TiO₂-APTS-3_CHO**

displayed 70.3 % and 76.9 % of degradation, respectively. As can be seen in Fig. 10a, the blank experiment, without photocatalyst, showed very low degradation ratio of MO under visible light irradiation (7.3 % after 150 min). So, the rate of degradation decreased for bare TiO_2 and **TiO_2-APTS-3_{CHO}** photocatalysts in the presence of visible light in comparison to use UV light; however, in the case of **TiO_2-3_{COOH}** 79.9 % of OM degradation occurred under visible light. The degradations of MO also followed a pseudo-first-order kinetics (Fig. 10b) and the reaction rate constant calculated for **TiO_2-3_{COOH}** using visible light (0.0097 min^{-1}) was 4.2 times higher than that achieved by unmodified TiO_2 (0.0023 min^{-1}) and 2.5 times greater than that reached with **TiO_2-APTS-3_{CHO}** (0.0038 min^{-1}). The photocatalyst concentration was also evaluated in order to enhance OM removal (Fig. 10c and 10d). As can be seen in Fig. 10c, the adsorption capacity of MO on sensitized TiO_2 nanoparticles was increased (about 20 %) when the photocatalyst load was increased to 1 g L^{-1}. Accordingly, the complete degradation of MO was reached in 60 min for **TiO_2-3_{COOH}** ($k = 0.057$ min^{-1}) and after 150 min **TiO_2-APTS-3_{CHO}** ($k = 0.022$ min^{-1}) (Fig. 10d).

In addition, the photoluminescence spectroscopy was recorded to study the recombination of photo-induced charge carriers in the synthetized TiO_2 samples (Fig. S33). Thus, a sharp drop in the PL intensity was observed when the TiO_2 material was sensitized with **3_{COOH}** and **3_{CHO}** compounds, which means the fluorescence was quenched by the surface modification, which involves a reduction in the electron-hole recombination rate. The reduction reached a 70 % of quenching in **TiO_2-3_{COOH}** material regarding TiO_2 material. This quenching effect is slightly less pronounced in the case of **TiO_2-APTS-3_{CHO}** sample where the fluorescence is quenched around the 50 %.

The interface charge transfer and charge separation efficiency of TiO_2 samples were also investigated by electrochemical impedance spectroscopy (EIS) measurements. Fig. S34a displays the Nyquist plots for the three photocatalysts where a small semicircle at high frequencies and a straight sloping line at low frequencies attributed to diffusional impedance can be observed. As can be seen, the radius of the arcs on the Nyquist plots of both dye-sensitized TiO_2 samples are smaller than that of the TiO_2 counterpart, indicating that charge transfer was considerably improved after TiO_2 functionalization. The Bode diagram (see Fig. S34b) shows the IR drop in the sensitized samples at low frequency. At this point, the capacitive behavior is not ideal, a sharp increase in the

impedance values takes place and the samples behave differently. The bare TiO_2 sample shows the highest impedance while the modified samples possess the lowest one. According to the EIS results, the presence of dyes in TiO_2 surface improves the charge separation efficiency and inhibits the electron-hole pair recombination [45, 46]. This result corresponds well with the signal decrease on PL spectra of sensitized TiO_2 materials in comparison to TiO_2 sample. Thus, the enhanced photocatalytic activity of sensitized TiO_2 nanoparticles with 3_{COOH} and 3_{CHO} compounds in comparison to bare TiO_2 nanoparticles can be explained by the synergetic effect of a narrower band gap, an optimal charge separation and a lower recombination rate of generated electron-hole pairs.


Fig. 10. Photocatalytic degradation of OM using TiO_2 samples. (a), (b) Comparison between using UV or visible lights and (c), (d) using catalyst load of 1 g L^{-1} under visible light.

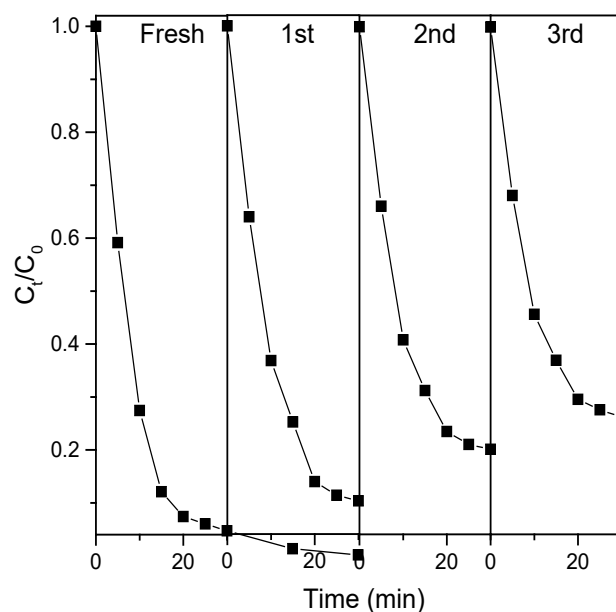1　　　**3.3.3. Stability and reusability and studies**

2　　　Photocatalysts were recovered by filtration and washed with water and then dried

3　in vacuum. The stability of photocatalysts was examined by FT-IR. Fig. S35 displays FT-IR

4　spectra of fresh and recovered photocatalysts after the degradation of MB and MO

5　under UV and visible irradiation. Comparing the spectra, the characteristic bands

6　corresponding to TSB compounds were observed in all the spectra. The reusability of

7　**TiO_2-3$_{COOH}$** was studied in the degradation of MB under visible irradiation and

8　degradation of MO under UV irradiation. As can be seen in Fig. 11, the MO removal

9　degradation was maintained for three runs, and only decreased slightly in the fourth

10　run. When visible light is applied, a moderate dropping of photocatalytic activity was

11　observed after three runs (Fig. 12).
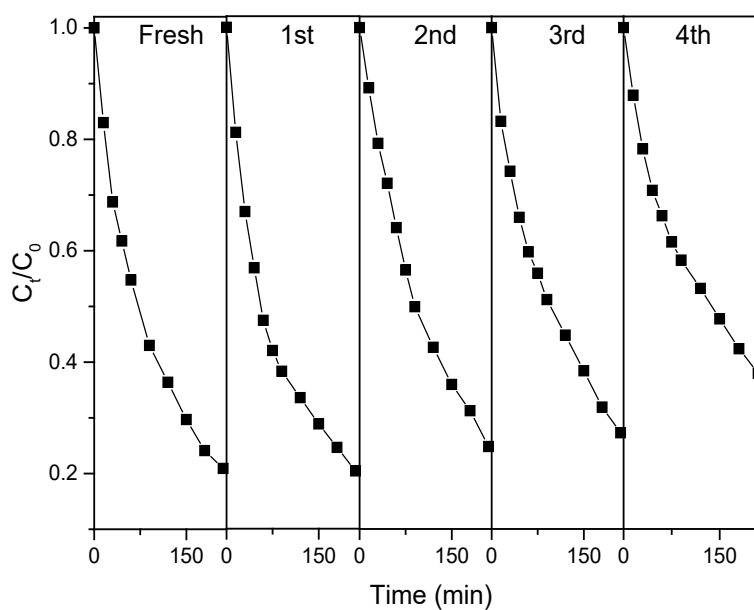
12

13　**Fig. 11.** Reusability of **TiO_2-3$_{COOH}$** in the degradation of MO under UV irradiation

3.3.4. Role of radical scavengers in photocatalyst activity and proposed mechanisms.

Photodegradation reactions were carried out, in the presence of different scavengers (2 mM), to analyze the role of primary reactive species involved in the degradation of MB. Benzoquinone (BQ), terc-butanol (t-BuOH) and ascorbic acid (AA) were used to scavenge superoxide free radicals ($\cdot O_2^-$), hydroxyl free radicals ($\cdot OH^-$) and positive holes (h$^+$), respectively. Authors have proved the similar effect of using scavengers in the photodegradation of different organic molecules, independently of their nature [47]. Generally, the addition of different scavengers had the same trend when the reaction was catalyzed by both materials, but the effect was not so marked in the case of **TiO$_2$-APTS-3$_{CHO}$** catalyst (Fig. S36). The addition of ascorbic acid as scavenger to the degradation reaction meant a more pronounced decrease in both materials (from 93.3 % to 48 % with **TiO$_2$-3$_{COOH}$** and from 93 % to 69 % with **TiO$_2$-APTS-3$_{CHO}$**). These results indicate that positive holes are the primary reactive species in photodegradation of MB, followed by superoxide free radicals, in whose experiment the degradation decreased from 93.3 % to 60.0 % with the **TiO$_2$-3$_{COOH}$** material. Differences between both catalysts can be related by the different sensitization mechanism. In type-II material, the

1 direct electronic injection from HOMO orbital of **3_COOH** dye to the valence band of TiO_2

2 is faster than for Type I material and the main reactive species involved in the

3 degradation are caught by the scavengers; therefore, when ascorbic acid and

4 benzoquinone were used the degradation ratios were lower. Thus, the proposed

5 mechanism is shown in Scheme 2.
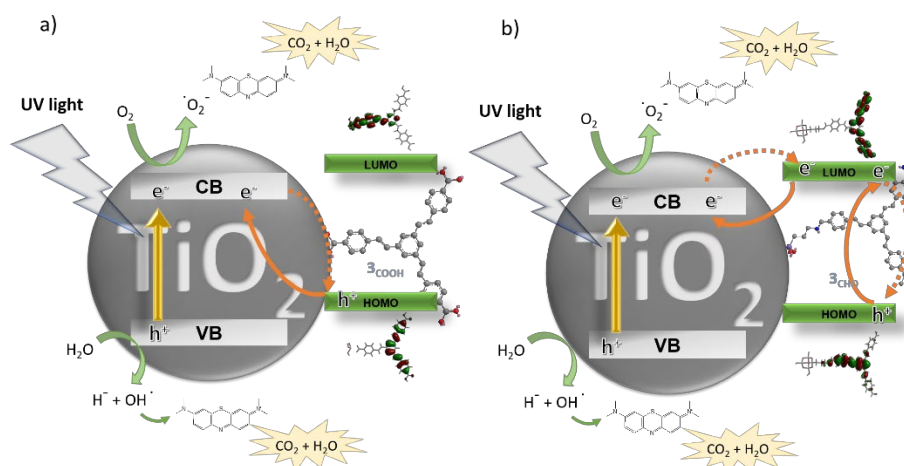
6

7 **Scheme 2.** Proposed mechanism of MB degradation under UV light using a) **TiO₂-3_COOH**

8 photocatalyst and b) **TiO₂-APTS-3_CHO** photocatalyst

9

10 When the UV irradiation falls upon TiO_2 surface, electrons of valence band can be

11 excited to the conduction band where can react with oxygen molecules to form

12 superoxide free radicals, which decompose MB molecules. Also, electrons situated at

13 HOMO level are also excited with the UV light through two different processes to

14 conduction band of TiO_2, via direct electronic injection for **TiO₂-3_COOH** and through LUMO

15 level of dye in the case of **TiO₂-APS-3_CHO**. Meanwhile, the photogenerated positive holes

16 in TiO_2 CB and dye HOMO levels oxidize water molecules to generate hydroxyl radicals,

17 which react with MB molecules to form into $CO_2 + H_2O$.

18 With the aim to elucidate the behavior under visible light irradiation, some

19 experiments using the same scavengers were also carried out in the photodegradation

20 of MB when **TiO₂-3_COOH** was used as catalyst (Fig. S36). A more pronounced drop in

21 photodegradation percentage was caused when ascorbic acid was added into the

22 reaction vessel, decreasing up to 38.0 %, that means photogenerated positive holes are

23 also the primary reactive species in this process. In the same way as ascorbic acid, a

24 higher decrease of degradation percentage was produced when BQ scavenger is added;

therefore, superoxide free radicals are also important reactive species in MB removal. The decrease of degradation percentages using VIS light is more marked compared to using UV light which suggests that a larger number of positive holes and superoxide radicals are produced during the visible photodegradation, which enhances the activity under visible light.

The proposed mechanism of photodegradation of MB under visible light irradiation is different to proposed under UV light (see Scheme 3). Thus, the compound anchored to TiO_2 (**3$_{COOH}$** dye) gets excited rather than the TiO_2 particles, so photons of visible light fall upon the **3$_{COOH}$** dye and the electrons are injected from dye HOMO level to the TiO_2 CB. There, the electrons can react with the adsorbed oxygen molecules to generate oxidizing species, like superoxide free radicals (O_2^-) which are capable of decomposing the MB molecules in a quick and non-selectively way [17, 34, 48]. Superoxide free radicals could also generate other oxidizing species that contribute to the degradation process (hydroperoxyl and hydroxyl radicals) [49]. Also, photogenerated positive holes in HOMO level of **3$_{COOH}$** dye are one of the main reactive species that can also degrade the MB molecules themselves [34]. In all this process, TiO_2 material acts as an electron-transfer mediator, even without being excited [49]. Thus, the sensitization of TiO_2 nanoparticles increases considerably the photocatalytic activity of bare TiO_2, due to the synergetic process between photogenerated positive holes in dye HOMO level and formed superoxide free radicals in TiO_2 CB.
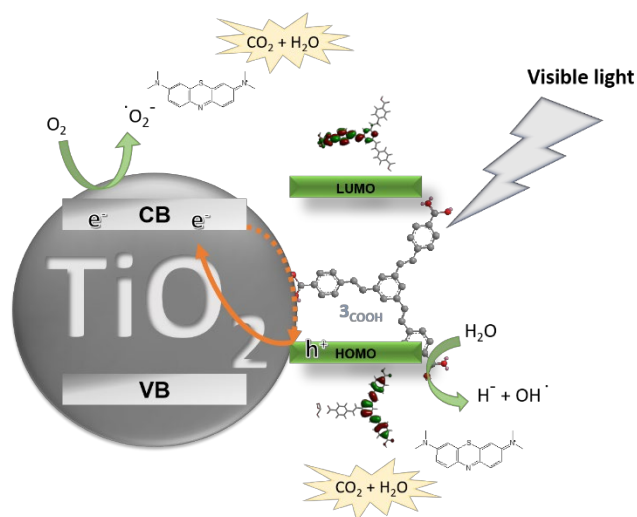
Scheme 3. Proposed mechanism of photocatalytic degradation of MB under visible light using **TiO_2-3$_{COOH}$**.

Finally, to get a deep insight in the degradation process, the mineralization efficiency of MB and MO molecules was calculated by TOC measurements. Fig. S37 shows the mineralization percentages of some photocatalytic experiments of MB (blue bars) and MO (orange bars) under UV and Vis lights irradiation. As can be seen, the TOC removal efficiencies of sensitized TiO_2 samples were greater than that of naked TiO_2 when UV light was used due to their effectiveness in the photocatalytic degradation. Differences between TiO_2-3$_{COOH}$ and TiO_2-APTS-3$_{CHO}$ materials in MB mineralization could be related to the reactive species involved in the process, which are more active when TiO_2-3$_{COOH}$ photocatalyst was utilized, as the scavengers' experiments elucidated. These good results in mineralization percentage are extrapolated to the photocatalytic experiments performed under visible light, not only for MB but also for MO degradation. The photogenerated oxidizing species like superoxide free radicals, among others, could successfully mineralize both MB and MO molecules and decompose them into more oxidized organic compounds and finally into CO_2 and H_2O molecules [48, 50].

4. Conclusions

Photocatalysts based on sensitized TiO_2 nanoparticles have been prepared for degradation of dye pollutants in water under both UV and visible light irradiation. The incorporation of TSB compounds on TiO_2 nanoparticles have shown to be efficient for enhancing UV and visible photocatalytic activity in the degradation of dye pollutants. **TiO_2-3$_{COOH}$** degraded MB dye 6.2 times faster than bare TiO_2 nanoparticles under visible light irradiation. The enhanced photocatalytic activity of **TiO_2-3$_{COOH}$** can be ascribed to the synergy between a direct electron transfer mechanism and a lower electron-hole recombination resulting an increase the lifetime of the electron-hole pairs. Based on the results of this study, the sensitized TiO_2 nanoparticles prepared could be also used for applications as water splitting and solar cells.

5. Acknowledgements

1   and the Universidad de Castilla-La Mancha for additional support of the research group

2   (Grant Nos. GI20163441, GI20173955, 2019-GRIN-27152).

3

References

[1] Rasheed T, Bilal M, Nabeel F, Adeel M, Iqbal HMN. Environmentally-related contaminants of high concern: Potential sources and analytical modalities for detection, quantification, and treatment. Environ Int. 2019;122:52-66. https://doi.org/10.1016/j.envint.2018.11.038

[2] Reza KM, Kurny ASW, Gulshan F. Parameters affecting the photocatalytic degradation of dyes using TiO_2: a review. Appl Water Sci. 2017;7(4):1569-78. https://doi.org/10.1007/s13201-015-0367-y

[3] Bilal M, Rasheed T, Nabeel F, Iqbal HMN, Zhao Y. Hazardous contaminants in the environment and their laccase-assisted degradation − A review. J Environ Manage. 2019;234:253-64. https://doi.org/10.1016/j.jenvman.2019.01.001

[4] Trawiński J, Skibiński R. Rapid degradation of clozapine by heterogeneous photocatalysis. Comparison with direct photolysis, kinetics, identification of transformation products and scavenger study. Sci Total Environ. 2019;665:557-67. https://doi.org/10.1016/j.scitotenv.2019.02.124

[5] Pelaez M, Nolan NT, Pillai SC, Seery MK, Falaras P, Kontos AG, et al. A review on the visible light active titanium dioxide photocatalysts for environmental applications. Appl Catal B Environ. 2012;125:331-49. https://doi.org/10.1016/j.apcatb.2012.05.036

[6] Zhang L, Cole JM. Anchoring Groups for Dye-Sensitized Solar Cells. ACS Appl Mater Interfaces. 2015;7(6):3427-55. https://doi.org/10.1021/am507334m

[7] Materna KL, Crabtree RH, Brudvig GW. Anchoring groups for photocatalytic water oxidation on metal oxide surfaces. Chem Soc Rev. 2017;46(20):6099-110. http://dx.doi.org/10.1039/C7CS00314E

[8] Rico-Santacruz M, Sepúlveda ÁE, Serrano E, Lalinde E, Berenguer JR, García-Martínez J. Organotitanias: a versatile approach for band gap reduction in titania based materials. J Mater Chem C. 2014;2(44):9497-504. http://dx.doi.org/10.1039/C4TC01704H

[9] Zhang G, Kim G, Choi W. Visible light driven photocatalysis mediated via ligand-to-metal charge transfer (LMCT): an alternative approach to solar activation of titania. Energ Environ Sci. 2014;7(3):954-66. http://dx.doi.org/10.1039/C3EE43147A

[10] Duan M-y, Li J, Mele G, Wang C, Lü X-f, Vasapollo G, et al. Photocatalytic Activity of Novel Tin Porphyrin/TiO2 Based Composites. J Phys Chem C. 2010;114(17):7857-62. https://doi.org/10.1021/jp911744a

[11] Min KS, Kumar RS, Lee JH, Kim KS, Lee SG, Son Y-A. Synthesis of new TiO_2/porphyrin-based composites and photocatalytic studies on methylene blue degradation. Dyes Pigments. 2019;160:37-47. https://doi.org/10.1016/j.dyepig.2018.07.045

[12] Yang C, Dong W, Cui G, Zhao Y, Shi X, Xia X, et al. Highly-efficient photocatalytic degradation of methylene blue by PoPD-modified TiO2nanocomposites due to photosensitization-synergetic effect of TiO2 with PoPD. Sci Rep. 2017;7(1):3973. https://doi.org/10.1038/s41598-017-04398-x

[13] Abou-Gamra ZM, Ahmed MA. Synthesis of mesoporous TiO_2–curcumin nanoparticles for photocatalytic degradation of methylene blue dye. J Photochem Photobiol B. 2016;160:134-41. https://doi.org/10.1016/j.jphotobiol.2016.03.054

[14] Shang X, Li B, Li C, Wang X, Zhang T, Jiang S. Preparation and enhanced visible light catalytic activity of TiO_2 sensitized with Benzimidazolone Yellow H3G. Dyes Pigments. 2013;98(3):358-66. https://doi.org/10.1016/j.dyepig.2013.03.009

[15] Phongamwong T, Donphai W, Prasitchoke P, Rameshan C, Barrabés N, Klysubun W, et al. Novel visible-light-sensitized Chl-Mg/P25 catalysts for photocatalytic degradation of rhodamine B. Appl Catal B Environ. 2017;207:326-34. https://doi.org/10.1016/j.apcatb.2017.02.042

[16] Chen F, Zou W, Qu W, Zhang J. Photocatalytic performance of a visible light TiO_2 photocatalyst prepared by a surface chemical modification process. Catal Commun. 2009;10(11):1510-3. https://doi.org/10.1016/j.catcom.2009.04.005

[17] Jiang Y, Meng L, Mu X, Li X, Wang H, Chen X, et al. Effective TiO_2 hybrid heterostructure fabricated on nano mesoporous phenolic resol for visible-light photocatalysis. J Mater Chem. 2012;22(44):23642-9. http://dx.doi.org/10.1039/C2JM35042D

[18] Ghanbari M, Bazarganipour M, Salavati-Niasari M. Photodegradation and removal of organic dyes using cui nanostructures, green synthesis and characterization. Sep Purif Technol. 2017;173:27-36. https://doi.org/10.1016/j.seppur.2016.09.003

[19] Mehdizadeh P, Orooji Y, Amiri O, Salavati-Niasari M, Moayedi H. Green synthesis using cherry and orange juice and characterization of $TbFeO_3$ ceramic nanostructures and their application as photocatalysts under UV light for removal of organic dyes in water. J Clean Prod. 2020;252:119765. https://doi.org/10.1016/j.jclepro.2019.119765

[20] Orooji Y, Ghanbari M, Amiri O, Salavati-Niasari M. Facile fabrication of silver iodide/graphitic carbon nitride nanocomposites by notable photo-catalytic performance through sunlight and antimicrobial activity. J Hazard Mater. 2020;389:122079. https://doi.org/10.1016/j.jhazmat.2020.122079

[21] Jamal Sisi A, Fathinia M, Khataee A, Orooji Y. Systematic activation of potassium peroxydisulfate with ZIF-8 via sono-assisted catalytic process: Mechanism and ecotoxicological analysis. J Mol Liq. 2020;308:113018. https://doi.org/10.1016/j.molliq.2020.113018

[22] Joaquin CG-M, Enrique D-B, Julian R-L. Conjugated Dendrimers with oly(Phenylenevinylene) and Poly(Phenyleneethynylene) Scaffolds. Curr Org Synt. 2008;5(3):267-90. http://dx.doi.org/10.2174/157017908785133438

[23] Tolosa J, Serrano de las Heras G, Carrión B, Segura T, Páez PL, de Lera-Garrido FJ, et al. Structure-Activity Relationships for Poly(phenylene)vinylene Derivatives as Antibacterial Agents. ChemistrySelect. 2018;3(25):7327-32. https://doi.org/10.1002/slct.201801287

[24] Díez-Barra E, García-Martínez JC, Merino S, del Rey R, Rodríguez-López J, Sánchez-Verdú P, et al. Synthesis, Characterization, and Optical Response of Dipolar and Non-Dipolar Poly(phenylenevinylene) Dendrimers. J Org Chem. 2001;66(17):5664-70. https://doi.org/10.1021/jo015764r

[25] Ortiz-Bustos J, Fajardo M, del Hierro I, Pérez Y. Versatile titanium dioxide nanoparticles prepared by surface-grown polymerization of polyethylenimine for photodegradation and catalytic CC bond forming reactions. Mol Catal. 2019;475:110501. https://doi.org/10.1016/j.mcat.2019.110501

[26] Frisch MJ, Trucks GW, Schlegel HB, Scuseria GE, Robb MA, Cheeseman JR, et al. Gaussian 09 Rev. B.01. Wallingford, CT2009.

[27] Cruz P, Fajardo M, del Hierro I, Pérez Y. Selective oxidation of thioanisole by titanium complexes immobilized on mesoporous silica nanoparticles: elucidating the environment of titanium(iv) species. Catal Sci Technol. 2019;9(3):620-33. http://dx.doi.org/10.1039/C8CY01929K

[28] Li J-G, Ishigaki T, Sun X. Anatase, Brookite, and Rutile Nanocrystals via Redox Reactions under Mild Hydrothermal Conditions: Phase-Selective Synthesis and Physicochemical Properties. J Phys Chem C. 2007;111(13):4969-76. https://doi.org/10.1021/jp0673258

[29] Byrne C, Subramanian G, Pillai SC. Recent advances in photocatalysis for environmental applications. J Environ Chem Eng. 2018;6(3):3531-55. https://doi.org/10.1016/j.jece.2017.07.080

[30] Jiang Z, Liu Y, Jing T, Huang B, Wang Z, Zhang X, et al. Enhancing visible light photocatalytic activity of TiO_2 using a colorless molecule (2-methoxyethanol) due to hydrogen bond effect. Appl Catal B- Environ. 2017;200:230-6. https://doi.org/10.1016/j.apcatb.2016.07.009

[31] Anwander R. SOMC@PMS. Surface Organometallic Chemistry at Periodic Mesoporous Silica. Chem Mater. 2001;13(12):4419-38. https://doi.org/10.1021/cm0111534

[32] de Lera-Garrido F, Sánchez-Ruiz A, Rodríguez-López J, Tolosa J, García-Martínez JC. Enhancement of emission by surfactant-induced aggregation in poly(phenylenevinylene)-based lipochromophores. Dyes Pigments. 2020;179:108410. https://doi.org/10.1016/j.dyepig.2020.108410

[33] Coya C, Álvarez AL, Ramos M, Andrés Ad, Zaldo C, Gómez R, et al. A fluorescent stilbenoid dendrimer for solution-processed blue light emitting diodes: SPIE, 2008.

[34] Bai X, Yang L, Hagfeldt A, Johansson EMJ, Jin P. D35-TiO_2 nano-crystalline film as a high performance visible-light photocatalyst towards the degradation of bis-phenol A. Chem Eng J. 2019;355:999-1010. https://doi.org/10.1016/j.cej.2018.08.061

[35] Moral M, Dominguez R, Fernandez-Liencres MP, Garzon-Ruiz A, Garcia-Martinez JC, Navarro A. Photophysical features and semiconducting properties of propeller-shaped oligo(styryl)benzenes. J Chem Phys. 2019;150(6):064309.

[36] García G, Granadino-Roldán JM, Garzón A, Moral M, Peña-Ruiz T, Navarro A, et al. Theoretical Study of Bis(phenylethynyl)thienoacenes as Precursors of Molecular Wires for Molecular Electronics. J Phys Chem C. 2010;114(28):12325-34. https://doi.org/10.1021/jp102345d

[37] Granadino-Roldán JM, Garzón A, García G, Peña-Ruiz T, Fernández-Liencres MP, Navarro A, et al. Theoretical study of the effect of ethynyl group on the structure and electrical properties of phenyl-thiadiazole systems as precursors of electron-conducting materials. J Chem Phys. 2009;130(23):234907. https://doi.org/10.1063/1.3149856

[38] Rienstra-Kiracofe JC, Tschumper GS, Schaefer HF, Nandi S, Ellison GB. Atomic and Molecular Electron Affinities: Photoelectron Experiments and Theoretical Computations. Chem Rev. 2002;102(1):231-82. https://doi.org/10.1021/cr990044u

[39] Nguyen CH, Fu C-C, Juang R-S. Degradation of methylene blue and methyl orange by palladium-doped TiO_2 photocatalysis for water reuse: Efficiency and degradation pathways. J Clean Prod. 2018;202:413-27. https://doi.org/10.1016/j.jclepro.2018.08.110

[40] Khan H, Rigamonti MG, Boffito DC. Enhanced photocatalytic activity of Pt-TiO_2/WO_3 hybrid material with energy storage ability. Appl Catal B Environ. 2019;252:77-85. https://doi.org/10.1016/j.apcatb.2019.04.019

[41] Ahmed MA, Abou-Gamra ZM, Salem AM. Photocatalytic degradation of methylene blue dye over novel spherical mesoporous Cr_2O_3/TiO2 nanoparticles prepared by sol-gel using octadecylamine template. J Environ Chem Eng. 2017;5(5):4251-61. https://doi.org/10.1016/j.jece.2017.08.014

[42] Santhi K, Navaneethan M, Harish S, Ponnusamy S, Muthamizhchelvan C. Synthesis and characterization of TiO_2 nanorods by hydrothermal method with different pH conditions and their photocatalytic activity. Appl Surf Sci. 2020;500:144058. https://doi.org/10.1016/j.apsusc.2019.144058

[43] Delsouz Khaki MR, Shafeeyan MS, Raman AAA, Daud WMAW. Evaluating the efficiency of nano-sized Cu doped TiO_2/ZnO photocatalyst under visible light irradiation. J Mol Liq. 2018;258:354-65. https://doi.org/10.1016/j.molliq.2017.11.030

[44] Islam MT, Jing H, Yang T, Zubia E, Goos AG, Bernal RA, et al. Fullerene stabilized gold nanoparticles supported on titanium dioxide for enhanced photocatalytic degradation of methyl orange and catalytic reduction of 4-nitrophenol. J Environ Chem Eng. 2018;6(4):3827-36. https://doi.org/10.1016/j.jece.2018.05.032

[45] Yang C, Dong W, Cui G, Zhao Y, Shi X, Xia X, et al. Highly-efficient photocatalytic degradation of methylene blue by PoPD-modified TiO_2 nanocomposites due to photosensitization-synergetic effect of TiO2 with PoPD. Sci Rep. 2017;7(1):3973. https://doi.org/10.1038/s41598-017-04398-x

[46] Xiang Y, Wang X, Zhang X, Hou H, Dai K, Huang Q, et al. Enhanced visible light photocatalytic activity of TiO_2 assisted by organic semiconductors: a structure optimization strategy of conjugated polymers. J Mater Chem A. 2018;6(1):153-9. http://dx.doi.org/10.1039/C7TA09374H

[47] Kiwaan HA, Atwee TM, Azab EA, El-Bindary AA. Photocatalytic degradation of organic dyes in the presence of nanostructured titanium dioxide. J Mol Struct. 2020;1200:127115. https://doi.org/10.1016/j.molstruc.2019.127115

[48] Chiu Y-H, Chang T-FM, Chen C-Y, Sone M, Hsu Y-J. Mechanistic Insights into Photodegradation of Organic Dyes Using Heterostructure Photocatalysts. Catalysts. 2019;9(5):430. https://doi.org/10.3390/catal9050430

[49] Kumar SG, Devi LG. Review on Modified TiO_2 Photocatalysis under UV/Visible Light: Selected Results and Related Mechanisms on Interfacial Charge Carrier Transfer Dynamics. J Phys Chem A. 2011;115(46):13211-41. https://doi.org/10.1021/jp204364a

[50] Sadeghi Rad T, Khataee A, Pouran SR, Joo SW. The key role of free radicals generated from activation of H_2O_2, $S_2O_8^{2-}$ and ozone over chromium/cerium co-doped magnetite nanoparticles. Sep Purif Technol. 2020;239:116538. https://doi.org/10.1016/j.seppur.2020.116538